Received: 1 August 2021 | Revised: 24 December 2021 | Accepted: 29 December 2021

DOI: 10.1111/ffe.13651

ORIGINAL ARTICLE

FFEMS Fatigue & Fracture of Engineering Materials & Structures WILEY

Fatigue failure risk evaluation of bimetallic rolls in four-high hot rolling mills

Mohd Radzi Aridi | **Nao-Aki Noda** | **Yoshikazu Sano** | **Kakeru Takata** | **Zifeng Sun** | **Yasushi Takase**

Department of Mechanical Engineering, Kyushu Institute of Technology, Kitakyushu-shi, Japan

Correspondence
Nao-Aki Noda, Department of Mechanical Engineering, Kyushu Institute of Technology, 1-1 Sensui-cho, Tobata-ku, Kitakyushu-shi 804-8550, Japan.
Email: noda.naoaki844@mail.kyutech.jp

Abstract

In hot rolling mills, bimetallic rolls are used because of the excellent hardness and wear resistance by applying high-speed steel (HSS) and ductile casting iron (DCI). Because most of the previous studies focused on surface spalling, almost no study is available for internal fatigue failure based on the stress during the rolling. In this study, therefore, a three-dimensional finite element method is applied to investigate the rolling stress of the work roll in the four-high rolling mill. A suitable chamfer geometry in the backup roll is discussed as well as the standard wear profile by considering those effects on the fatigue. Then, to evaluate the fatigue risk under compressive mean stress, the fatigue limit lines in the stress amplitude versus mean stress diagram are newly discussed. With the aid of previous experience in industries, the fatigue fracture risk is discussed by focusing on three critical points inside the work roll.

KEYWORDS

bimetallic roll, fatigue failure, four-high rolling mill, roll profile, stress analysis

1 | INTRODUCTION

Hot rolling processes more tonnage than any other manufacturing process. The most important segments of a modern hot rolling mill are often related to the work rolls; and therefore, many studies have been conducted to improve wear resistance, surface resistance, and heat crack resistance of the work rolls.[1–3] To meet such different demands, roll manufactures have developed bimetallic rolls widely used to replace the conventional single material rolls.[4] Bimetallic rolls are manufactured by the centrifugal casting method, in which high-speed steel (HSS) is used as the outer layer and ductile casting iron (DCI) is used and the inner layer.[5] The bimetallic roll can be used more than 10 times longer than the high alloy grain rolls and high chromium rolls previously used.

Compared with the backup roll, the work roll surface is frequently ground with a smaller wear amount in order to use the surface repeatedly by removing surface roughness caused by wear during the use. For this reason, surface spalling caused by the crack initiated at the roll surface hardly occurs in works rolls although it often occurs in backup rolls. Although the outer surface damage is often removed in the bimetallic work rolls, the inner layer is consecutively used and therefore is subjected to a large number of load repetitions exceeding 10^7 times corresponding to the total life of the work roll. Small defects and abnormal microstructures near the HSS/DCI boundary layer appearing during the casting process can be the defect causing delamination under the repeated rolling loads. Because the recent work roll tends to be used for a longer period under severe conditions by applying high-strength materials, the fatigue fracture caused by the crack initiation at the inside of the roll is becoming important.

Figure 1 illustrates an example of internal fatigue failure considered in this paper. As shown in Figure 1A, in this high alloy grain roll, a semielliptical beach mark can be clearly seen near the grain/FC boundary at Point B. The beach mark proves that the fatigue crack initiates at the inner boundary Point A and propagates toward the surface.[6,7] Roll maker companies also identified that similar failure sometimes can be seen near the end of the roll body (see point B_{750}^{270} in Figure 12). Such peeling in Figure 1 is mainly caused by the variation of σ_r during the roll rotation. In this way, the internal failure focused in this study is totally different from the surface spalling, causing surface layer peeling observed in the backup rolls. This is because the spalling is mainly controlled by the repeated shear stress due to the rolling contact fatigue at several millimeters depth from the roll surface. Considering those situations, the authors have been keenly aware of the necessity for considering the entire roll space instead of just focusing on the surface spalling. Then, the fatigue failure risk should be evaluated on the basis of the rolled stress clarified in this paper.

Therefore, in this study, the fatigue risk will be evaluated by clarifying the rolling stress appearing inside of the bimetallic work rolls when the work roll is used in a four-high rolling mill. It is necessary to consider the residual stress of the work roll in the final evaluation of fracture risk. However, the heat treatment conditions are different depending on each roll manufacture's company. Therefore, this study focuses on clarifying the rolling stress in the four-high rolling mill, which has not been studied until now. For this purpose, the residual stress is set to zero, and the fatigue fracture risk point will be clarified from the viewpoint of rolling stress.

2 | FINITE ELEMENT METHOD MODELING WITH FUNDAMENTAL DIMENSIONS

The seven-stand hot strip finishing mill has been commonly used in the steel industry for more than 50 years. Among them, the most severe usage of the roll at No.4 stand causes a relatively larger amount of wear and fatigue failure. Therefore, in this paper, the fatigue failure of the work roll at No.4 stand will be discussed because the fatigue of the backup roll hardly happens. This is partly because the backup roll material is close to bearing steel and resistant to wear and fatigue, and also, the backup roll surface is occasionally ground to remove the surface wear and fatigue layers. Moreover, after the work roll shifting method has been introduced, the stress concentration at the chamfered edge of the backup roll has been significantly reduced.

Figure 2 shows a three-dimensional (3D) finite element method (FEM) model of a four-high rolling mill. Here, the following dimensions are considered: the work roll diameter $D_W = 660\,\text{mm}$, the backup roll diameter $D_B = 1400\,\text{mm}$, and the body length for both rolls $L = 1800\,\text{mm}$, and the rolled steel width $W = 1200\,\text{mm}$ where the inlet thickness is 4.9 mm and the outlet thickness is 3.3 mm. The width dimension $W = 1200\,\text{mm}$ is commonly used and is recognized as a typical condition by many roll makers and steel companies. The work roll as well as the backup roll is subjected to the total rolling force P_{total} whose standard value is $P_{total} = 16400\,\text{kN}$.[8,9] Then, the work roll is subjected to the average line force $p_S^{ave} = P_{total}/W$ from the rolled steel. Also, the work roll is subjected to the average line force $p_B^{ave} = P_{total}/(L - \ell_c)$ from the backup roll. As shown in Figure 2, the backup roll is chamfered with a length of $\ell_c = 60\,\text{mm}$ and a depth

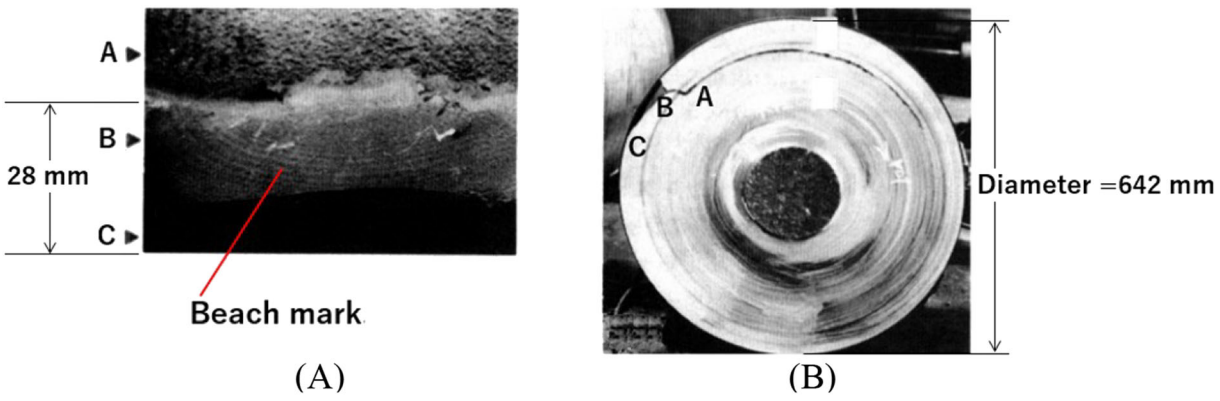

FIGURE 1 Roll failure where the crack originated at grain/FC boundary (grain, grain graphite; FC, flaky graphite cast iron) in bimetallic work roll and propagates towards the surface (A) fractured surface: A, near boundary; B, beach mark in shell; C, roll surface. (B) Cross-sectional view of spalling crack[6,7] [Colour figure can be viewed at wileyonlinelibrary.com]

of 20 mm.[10] The effect of the chamfer geometry on the work roll will be described in Section 4.

Figure 3 shows the stress–strain diagrams of HSS for the outer layer of the work roll and DCI for the inner layer of the work roll. In this paper, "the outer layer" is used to represent the whole outer region of the HSS/DCI boundary $r = 270\tilde{3}0$ mm, and "the inner layer" is used to represent the whole inner region of the HSS/DCI boundary $r = 02\tilde{7}0$ mm. Table 1 shows the material properties used in the analysis.[11] As shown in Table 1, high chrome steel is used for the backup roll. During one roll rotation, the thermal stress appears due to heating and cooling from the hot-rolled steel. However, it is known that the thermal stress affects only a few μm to 1 mm depth from the surface and never affects the inside boundary stress.[12,13] After the rolling starts, the roll temperature increases and becomes stable after 1 h under an equilibrium temperature of about 50 – 80°C.[7,14] Because the rolling operation is more than 10 h continuously before removing the damaged roll surface, the effect of thermal stress at the initial stage of rolling is relatively smaller and can be ignored when considering fatigue fracture.[7] Therefore, in this study, the thermal stress is not considered, and the analysis is performed at room temperature.

The FEM software MSC Marc/Mentat 2012 is used for the 3D elastoplastic contact analysis although it is not clear whether plastic deformation occurs or not in the internal region of the work roll. The stress–strain curves of HSS and DCI in Figure 3 are used for the FEM elastoplastic contact analysis. The multi-linear isotropic hardening curves starting from the yield stress are applied. Then, Mises yield criterion is formulated in terms of the equivalent tensile stress. The FEM elements used are four-node tetrahedral elements and eight-node hexahedral elements for the stress concentration part. The direct constraint method is applied for the contact analysis between the work roll and backup roll. The total number of nodes is 22,320, and the total number of elements is 20,006 with the minimum element dimensions 30 × 30 × 30 mm. The accuracy of the stress around the HSS/DCI boundary can be estimated as less than 1% error from the mesh independence.

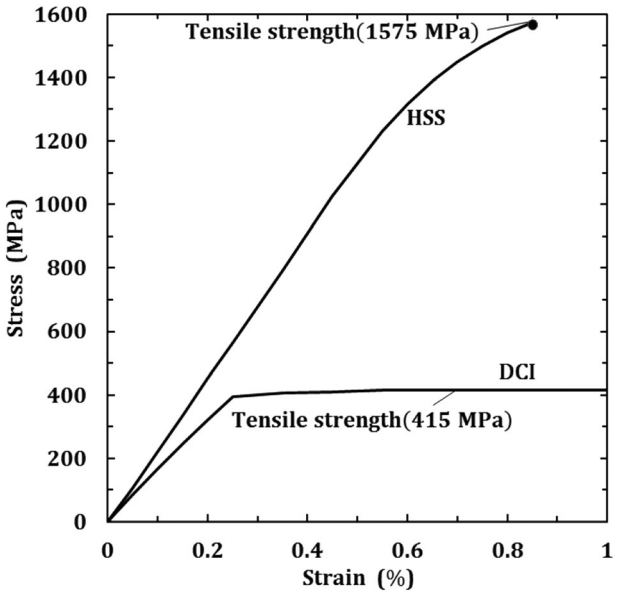

FIGURE 3 Stress–strain relation for HSS and DCI of the work roll

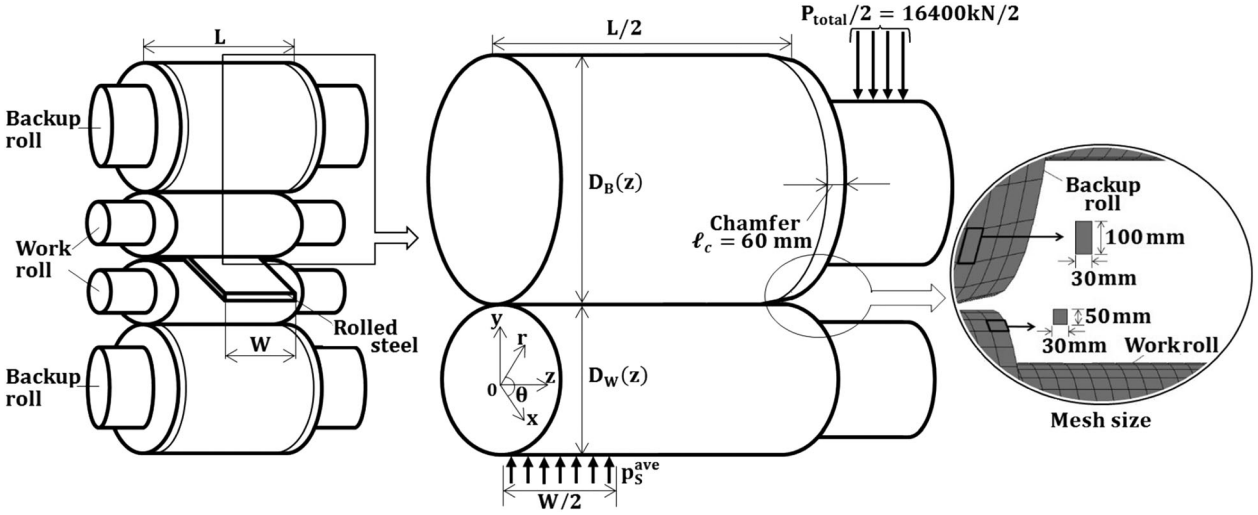

FIGURE 2 Three-dimensional FEM model of a four-high rolling mill

3 | STRESS VARIATION IN THE WORK ROLL DURING A ROLL ROTATION

With the aid of previous roll failures experienced in industries,[6–8] several critical points can be identified by applying FEM to the entire 3D space of the work roll. As mentioned in the previous section, because the crack originates near the HSS/DCI boundary and propagates along the r = constant surface, the stress amplitude of σ_r should be focused by considering the maximum stress amplitude.[6,15] In Section 3.1, because the stress amplitude is caused by the roll rotation, the stress variation in the θ-direction will be considered for the work roll. In Sections 3.2 and 3.3, the stress variations $\sigma_r, \sigma_\theta, \sigma_z$ with the yielding condition in the work roll will be discussed on the basis of fundamental roll dimensions where the backup roll's crown profile $h_c = 0$ and the work roll's wear profile $h_w = 0$. The effect of these roll profiles will be discussed later in Section 4.

TABLE 1 Material properties of the rolls

Property	HSS	DCI	Backup roll
Tensile strength (MPa)	1575	415	1575
Fatigue strength[a] (MPa)	630	166	630
Yield strength (MPa)	1270	410	-
Young's modulus (GPa)	230	174	210
Poisson's ratio	0.3	0.28	0.3
Density (kg/m^3)	7600	7300	7800

[a]Reference[11].

3.1 | Surface stress variation in the θ-direction of the work roll

Figure 4 illustrates the line forces $p_B(z)$ and p_S^{ave} commonly used in roll industries and also used in this analysis. Along the line θ = 90°, the work roll is subjected to the line force $p_B(z)$ from the backup roll. Along the line θ = −90°, the work roll is subjected to the line force p_S^{ave} from the rolled steel. The line force p_S^{ave} is insensitive to the work roll's wear profile but varies in the width direction of the rolled steel due to the temperature. However, because the analysis method is not generalized, in this paper, p_S^{ave} = constant is assumed.

Figure 5 shows the surface stress variation $\sigma_r, \sigma_\theta, \sigma_z$ at z = 0 in the θ-direction. The internal stress varies in a similar way in Figure 5 as described later (see Figures 6 and 7). Figure 5 shows that the target stress σ_r takes the maximum compressive stress at θ = −90° due to the contact of the rolled steel as well as σ_θ, σ_z. Those stresses take the secondary maximum compressive stresses at θ = 90° due to the contact of the backup roll. This is because the

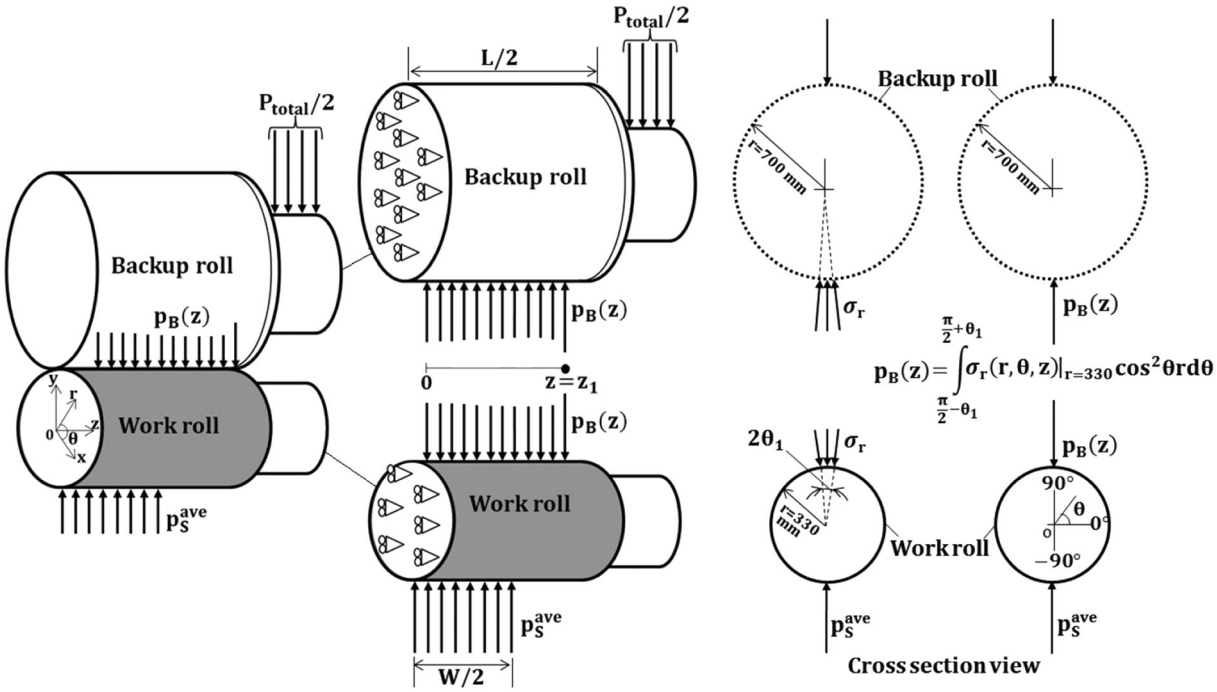

FIGURE 4 Definition of line force $p_B(z)$ from backup roll where the contact length $z_1 = L/2 - \ell_c$ in the z-direction and the contact angle θ_1 in the θ-direction where $\theta_1 \cong 1°$

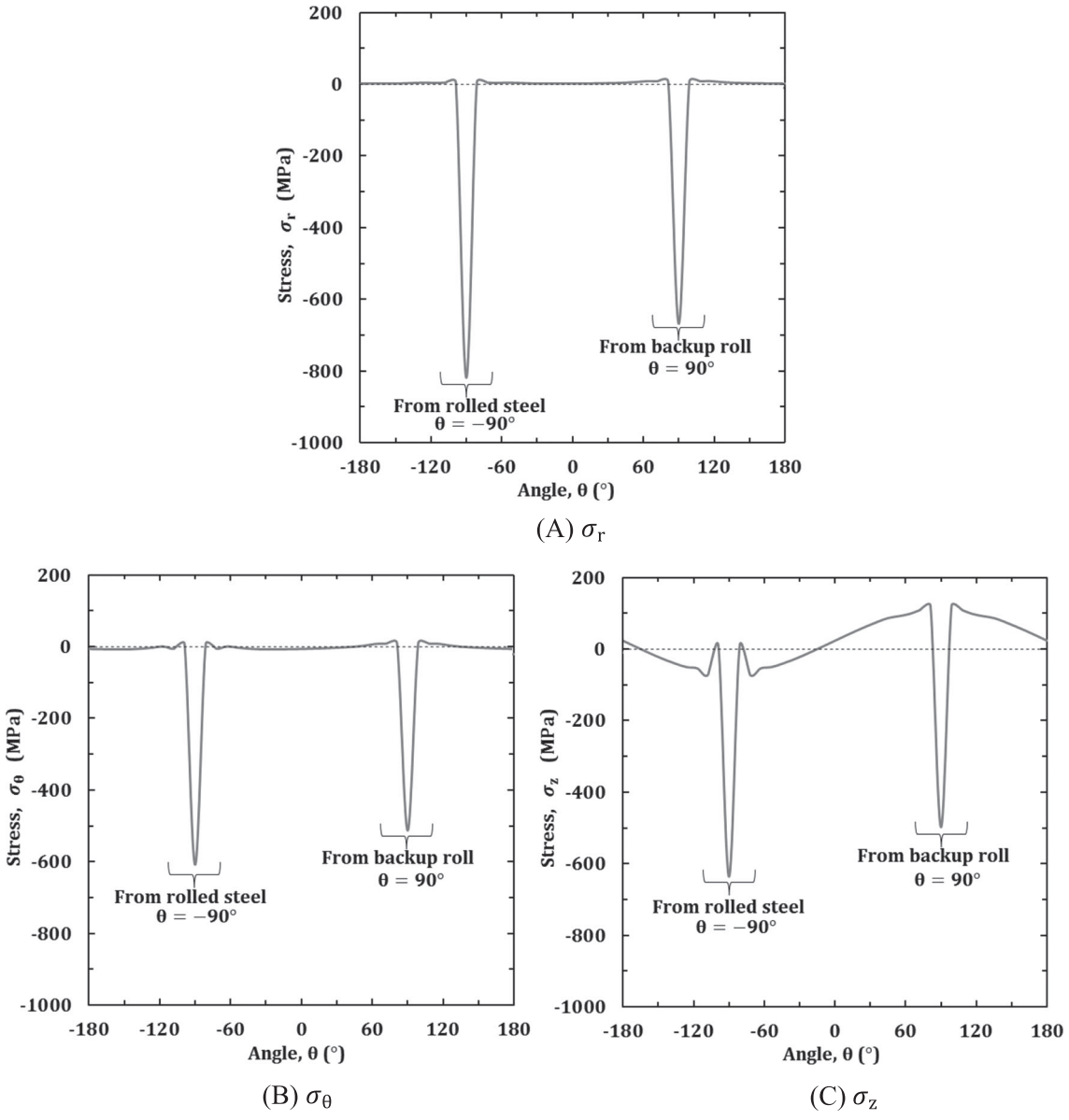

FIGURE 5 Surface stress variation in the θ-direction of the work roll at z = 0 in Figure 3: (A) stress σ_r, (B) stress σ_θ, (C) stress σ_z when $P/P_{total} = 1.0$

line force $p_S^{ave} = P_{total}/W$ from the rolled steel is larger than the line force $p_B^{ave} = P_{total}/L$ from the backup roll because W = 1200 mm is shorter than L = 1800 mm.

3.2 | Surface and HSS/DCI boundary stress variation in the z-direction of the work roll

Figure 6 compares the stress distributions on the surface r = 330 mm and on the HSS/DCI boundary r = 270 mm. As illustrated in Figure 6A, the stress along the five lines θ = −90°, −45°, 0°, 45°, 90° are focused on the roll surface and the HSS/DCI boundary to compare their stress distributions.

Figure 6B–D shows the stress variation σ_r, σ_θ, σ_z along the lines θ = −90°, −45°, 0°, 45°, 90° on the roll surface and HSS/DCI boundary. In the previous section, Figure 5 showed that the maximum surface compressive stress appears at θ = −90° and z = 0. Regarding the inside stress at the HSS/DCI boundary r = 270 mm, Figure 5 indicates that the maximum compressive stress appears at θ = −90° and the secondary maximum stress appears at θ = 90° similar to the surface stress. The maximum compressive stress σ_r is larger than σ_θ, σ_z. Furthermore, because the stress σ_r controls the HSS/DCI boundary

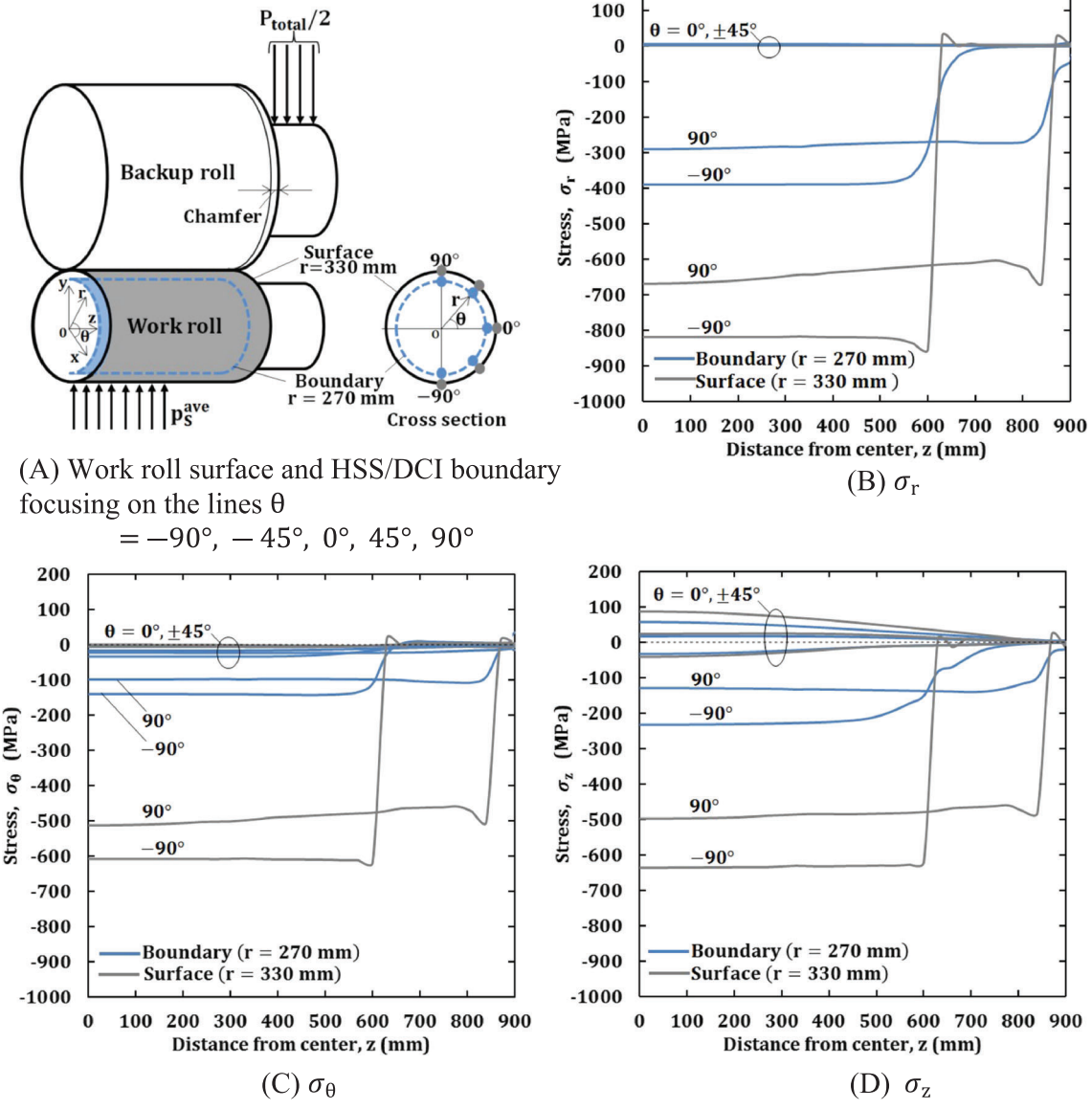

FIGURE 6 (A) Bimetallic work roll surface r = 330 mm and the HSS/DCI boundary r = 270 mm focusing on the lines θ = −90°, −45°, 0°, 45°, 90°, (B) stress σ_r, (C) stress σ_θ, (D) stress σ_z when $P/P_{total} = 1.0$ [Colour figure can be viewed at wileyonlinelibrary.com]

fatigue failure as shown in Figure 1A, in the following discussion, we will focus on the stress σ_r. At the roll surface r = 330 mm, the compressive stress $\sigma_r = 817$ MPa is lower than the yield stress 1270 MPa of HSS; and therefore, the yielding condition is not satisfied because all stress components $\sigma_r, \sigma_\theta, \sigma_z$ are compressive. Similarly, at the HSS/DCI boundary r = 270 mm, the compressive stress $\sigma_r = 388$ MPa is lower than the yield stress 410 MPa of DCI; and therefore, the yielding condition is not satisfied because all stress components $\sigma_r, \sigma_\theta, \sigma_z$ are compressive. Therefore, although elastoplastic contact analysis is performed, the plastic deformation does not appear in this study.

As shown in Figure 6, although the maximum compressive stress σ_r appears on the surface, in this study, the HSS/DCI boundary stress σ_r is focused because of the following reason. Compared with the backup roll, the work roll surface is frequently ground with a smaller wear amount in order to use the surface repeatedly by removing surface roughness caused by wear during the use. For this reason, surface spalling caused by the crack initiated at the roll surface hardly occurs in works rolls

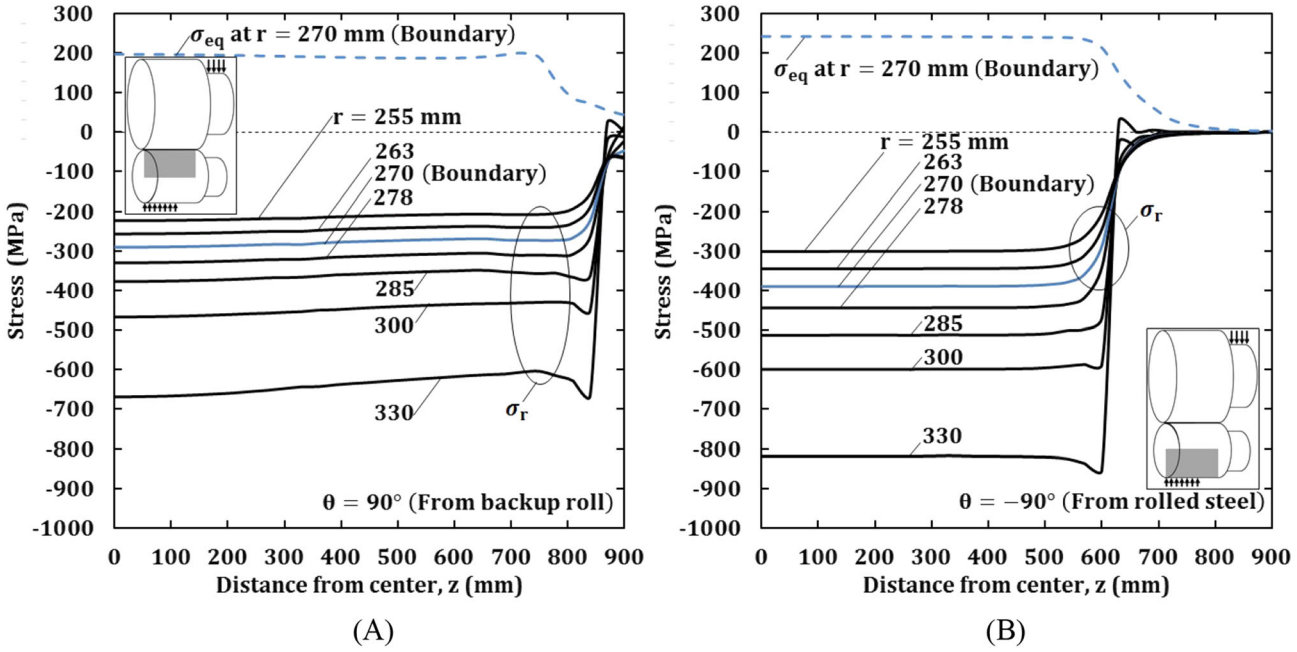

FIGURE 7 Stress variation σ_r (solid line) and σ_{eq} (dotted line) in the work roll when $P/P_{total} = 1.0$: (A) due to the contact with the backup roll, (B) due to the contact with the rolled steel [Colour figure can be viewed at wileyonlinelibrary.com]

although often occurring in backup rolls. As a matter of fact, the authors' previous investigation revealed that the work roll surface failure is not caused by normal fatigue but closely related to rolling troubles.[6,7] Instead, the backup rolls' spalling is usually caused by the fatigue crack initiated at a few mm depth from the surface under the repeated shear stress. Because the rolling contact fatigue and the spalling in backup rolls are controlled by the shear stress, they are totally different from the target of this study, that is, the HSS/DCI boundary failure controlled by repeated boundary stress σ_r.

3.3 | Stress variation σ_r in the vicinity of the HSS/DCI boundary of the work roll

In Section 3.3, as shown in Figure 1, because the HSS/DCI boundary failure is mainly caused by the stress σ_r, the variation of the stress σ_r is discussed. The equivalent Mises stress σ_{eq} is also considered to confirm the plasticity. Figure 7 illustrate σ_r variations denoted by the solid line in the range $255\,mm \le r \le 330\,mm$ including the HSS/DCI boundary $r = 270\,mm$ where equivalent Mises stress σ_{eq} is also indicated. Figure 7A illustrates the stress in the longitudinal section $\theta = 90°$ of the work roll due to the contact with the backup roll $0 \le z \le L/2 = 900\,mm$. A peak value of σ_r can be seen near the end of the contact area. Figure 7B illustrates the stress in the longitudinal section $\theta = -90°$ of the work roll due to the contact with the rolled steel $0 \le z \le W/2 = 600\,mm$. Also, a peak value of σ_r can be seen near the end of the contact area. From the comparison between Figure 7A and Figure 7B, the stress σ_r due to the contact from the rolled steel is larger. This is because the contact length $W/2 = 600\,mm$ is smaller than the one of $L/2 = 900\,mm$. The maximum internal stress σ_r in the section $\theta = -90°$ is the same as the surface stress σ_r in Figure 6B. The Mises stress at the boundary $r = 270\,mm$ in Figure 7A,B shows that the Mises stress value is much smaller than the yield stress 410 MPa of DCI; and therefore, the yielding condition is not satisfied and plastic deformation is not activated.

As shown in Figure 7A,B, the stress σ_r is largest at the surface; however, as mentioned in Sections 1 and 3.2, the surface spalling studied in backup roll does not happen in work rolls.[16–18] Although the crack initiation of the rolling fatigue is mainly controlled by shear stress at a few mm depth of the surface, the fatigue fracture treated in this study starts in the vicinity of the HSS/DCI boundary. In this failure, the stress amplitude of σ_r near the HSS/DCI boundary controls for the crack initiation and propagation as shown in Figure 1. In Section 4, the rolling condition will be determined to represent real rolling in the numerical simulation. Then, in Section 5, the internal stress σ_r at the HSS/DCI boundary at $r = 270\,mm$ will be mainly discussed to evaluate the fatigue failure risk from the inside roll because no study is available.

4 | EFFECT OF CHAMFER GEOMETRY IN BACKUP ROLL AND EFFECT OF WEAR PROFILE IN WORK ROLL

In Section 3, stress variations in work roll were discussed on the basis of fundamental roll dimensions. In Section 4.1, the effect of chamfer geometry in backup roll will be discussed by varying the roll chamfer length as $\ell_c = 30\tilde{1}20$ mm to obtain the suitable chamfer geometry. Then, in Section 4.2, by using the suitable chamfer length ℓ_c and varying the wear depth h_w as $h_w = 00\tilde{.}3$ mm under fixed crown height $h_c = 0.5$ mm, the typical wear profile will be discussed.

4.1 | Effect of chamfer geometry in backup roll on the surface shear stress

Figure 8A illustrates several chamfer geometries by varying the chamfer length as $\ell_c = 30, 60, 90,$ and 120 mm. Figure 8B shows the surface shear stress τ_{rz} controlling the crack initiation due to the rolling contact fatigue at the roll end. As mentioned above, in this paper, fatigue failure from the internal HSS/DCI boundary is focused, and the shear stress causing the crack initiation near the surface is not considered. However, in order to consider the optimum chamfer geometry, in this section, the shear stress is specially discussed. A certain amount of chamfer ℓ_c is necessary to avoid collision damage during roll handling. The surface shear stress τ_{rz} can be smallest when $\ell_c = 30$ mm; however, a larger chamfer length is necessary to reduce work roll bending by introducing the contact at the central portion of the rolls. In this sense, the chamfer length is $\ell_c = 60$ mm is chosen for the following analysis.

4.2 | Effect of wear profile in work roll on the line force $p_B(z)$

Next, the crown profile h_c in the backup roll diameter $D_B(z)$ in Figure 2 and the wear profile h_w in the work roll diameter $D_W(z)$ will be discussed. Thermal crown caused by the thermal expansion is not considered because thermal deformation is smooth enough compared with the wear profile having a negligible effect on the line force. In this study, the Equations 1 and 2 are applied to express the backup roll diameter $D_B(z)$ with crown height h_c and the work roll diameter $D_W(z)$ with the wear amount h_w (see Figure 9A).

$$D_B(z) = 1400 + 2h_c\sqrt{1 - z/\ell_b} \quad (1)$$

$$D_W(z) = 660 - 2h_w\sqrt{1 - z/\ell_a} \quad (2)$$

Here, ℓ_a is the length of the curved part of the work roll, and ℓ_b is the length of the curved part of the backup roll. Under the basic conditions, the amount of wear $h_w = 0$.

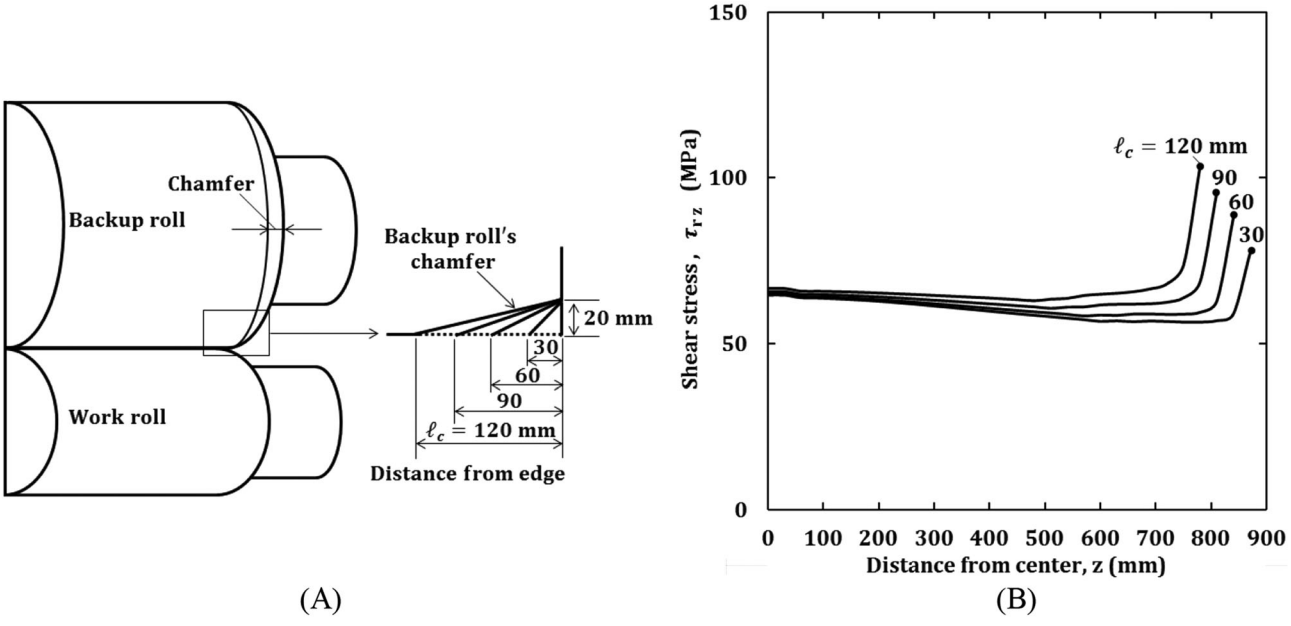

FIGURE 8 (A) Chamfer geometry at the edge of the backup roll; (B) surface shear stress to determine the chamfer geometry on the backup roll in (A) when the chamfer lengths $\ell_c = 30,\ 60,\ 90,\ 120$ mm from the edge under $P/P_{total} = 1.0$

In Equation 2, the wear profile changes slightly at the center of the wear $z \approx 0$ and changes largely near the wear end of wear $z \approx \ell_a$. The comparison shows that Equation 1 coincides with the circular arc shaped backup roll diameter expressed in Equation 3 within 0.12 mm.

$$D_B(z) = 1400 + 2h_c - 2\left[\frac{(h_c)^2 + (\ell_b)^2}{2h_c} - \sqrt{\left(\frac{(h_c)^2 + (\ell_b)^2}{2h_c}\right)^2 - z^2}\right] \quad (3)$$

An appropriate crown height h_c in Equation 1 can be determined in the following way. The bending deformation of the backup roll can be calculated from the deflection $\delta_{z=900}$ at the body end and the deflection $\delta_{z=0}$ at the body center as $\Delta\delta = \delta_{z=900} - \delta_{z=0} = 0.2$ mm. The maximum wear profile of the work roll can be estimated as $h_w = 0.3$ mm. Therefore, the crown amount of the backup roll h_c should be $h_c = \Delta\delta + h_w = 0.2\,\text{mm} + 0.3\,\text{mm} = 0.5\,\text{mm}$. Here, $\Delta\delta = \delta_{z=900} - \delta_{z=0} = 0.2$ mm is the backup roll's bending deformation, and $h_w = 0.3$ mm is the maximum wear appearing in the work roll.

The line force defined in Equations 4–7 is commonly used to express the external force applied to the work roll. In this section, the effect of the wear profile on the line force is clarified for the roll modelling. As shown in Figure 9A, by varying h_w, the effect of wear profile on the line force $p_B(z)$ is discussed by applying the 3D contact elastoplastic FEM analysis.

$$p_B(z) = \int_{\frac{\pi}{2}-\theta_1}^{\frac{\pi}{2}+\theta_1} \sigma_r(r,\theta,z)|_{r=330}\cos^2\theta r d\theta \quad (4)$$

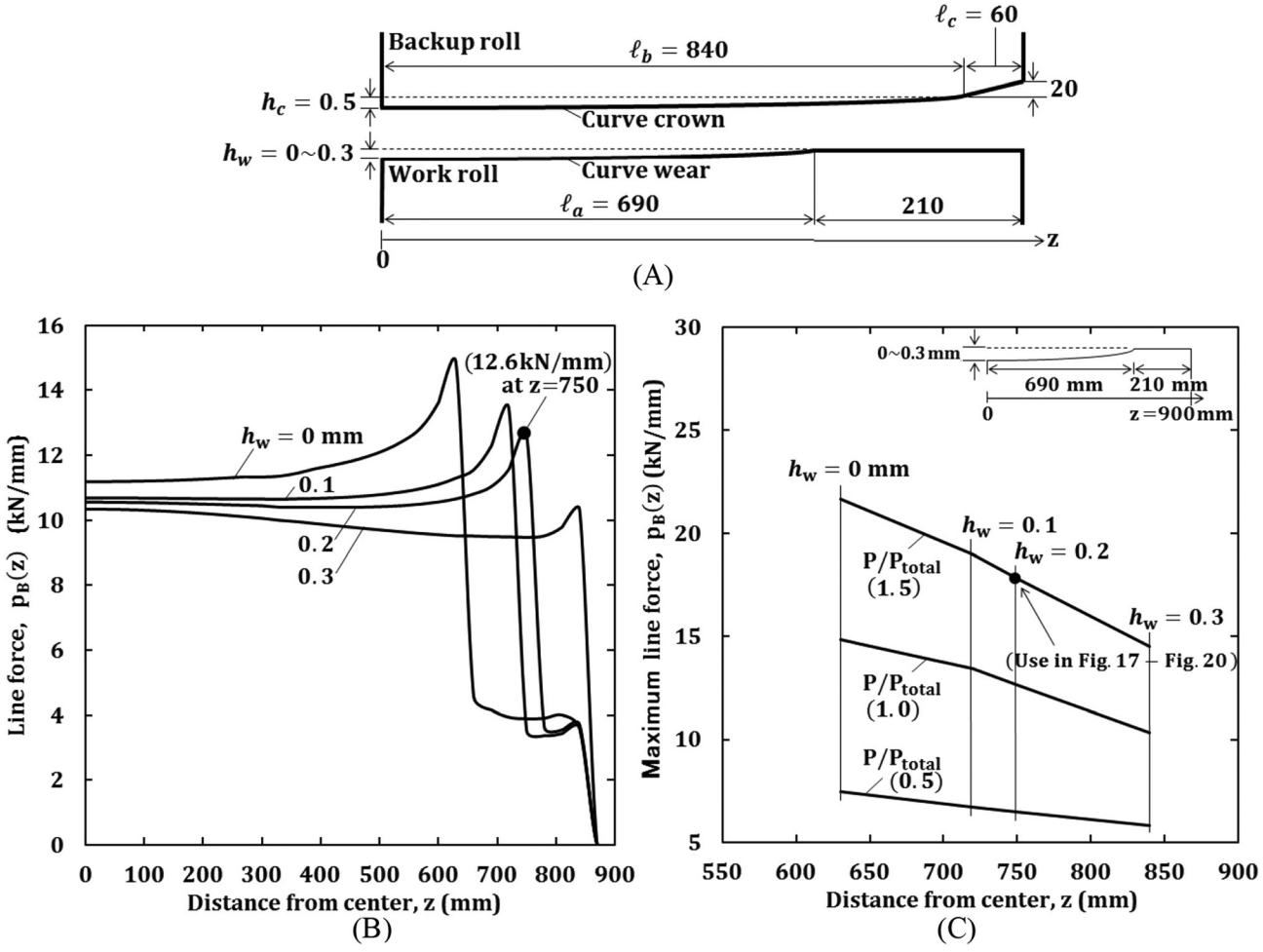

FIGURE 9 (A) Roll profiles illustration; (B) line force $p_B(z)$ from backup roll when $h_c = 0.5$ mm, $P/P_{total} = 1.0$, and $h_w = 0, 0.1, 0.2, 0.3$ mm; (C) maximum line force $p_B(z)$ applied from backup roll versus the position of the maximum line force when $P/P_{total} = 0.5, 1.0, 1.5$ and wear depth $h_w = 0,\ 0.1,\ 0.2,\ 0.3$ mm

Here, θ_1 is the angle of the contact area shown in Figure 4, and $\sigma_r|_{r=330}$ is the contact stress on the roll surface $(r = 330\,mm)$. In Equation 4, $\tau_{r\theta}(r,\theta,z)|_{r=330}$ is not included because the effect of shear stress is smaller because of the smaller contact angle $\theta_1 \cong 1^\circ$ although in the FEM analysis, the effect of shear stress on $p_B(z)$ is included. The total rolling force P can be defined in Equation 5.[19]

$$P = \int_0^{z_1} p_B(z)dz \tag{5}$$

Here, z_1 is the contact length where $z_1 = L/2 - \ell_c$ indicated in Figure 4. The average line forces p_B^{ave} and p_S^{ave} are defined in Equations 6 and 7.

$$p_B^{ave} = P/L \tag{6}$$

$$p_S^{ave} = P/W \tag{7}$$

Figure 9B shows the line force $p_B(z)$ along the contact area for different wear amounts h_w. The backup roll's crown height is fixed as $h_c = 0.5\,mm$, and the work roll's wear depth is changed as $h_w = 0, 0.1, 0.2, 0.3\,mm$. When the wear profile $h_w = 0$, the line force distribution $p_B(z)$ is the largest. With increasing h_w, the line force $p_B(z)$ decreases, and the largest position moves to the roll end. Figure 9C shows the maximum value of the line force $p_B(z)$ and the position when the rolling force ratio $P/P_{total} = 0.5, 1.0, 1.5$. Here, the rolling force ratio is set as $P/P_{total} = 0.5 - 1.5$. This is because the standard force $P/P_{total} = 1$ may vary depending on the setting error regarding the rolling material temperature, rolling force, and the impact force at the rolling trouble. As shown in Figure 9C, with increasing h_w, the maximum line force $p_B(z)$ decreases. As an example, the position of the peak line force is width $z = 630\,mm$ when $h_w = 0$. The peak position moves to the roll end. This is because the crown highest is largest at the roll center and gradually decreases toward the end roll. From the above discussion, for the analysis model, a relatively large amount of wear amount $h_w = 0.2\,mm$ is chosen to provide a relatively high maximum line force $p_B(z)$.

5 | FATIGUE RISK EVALUATION OF ROLLS UNDER STANDARD ROLLING PROFILE

As discussed in the previous section, the following profiles are assumed for typical roll modelling. Regarding the backup roll, the chamfer length is set to $\ell_c = 60\,mm$, and the crown amount is set to $h_c = 0.5\,mm$. Also, the work roll's wear amount is set to $h_w = 0.2\,mm$. For this section, even though the standard rolling force ratio is $P/P_{total} = 1.0$, a more severe ratio $P/P_{total} = 1.5$ is assumed to evaluate the fatigue failure risk when the rolling trouble happens such as the impact force due to the rolling plate biting and the temperature drop of the rolled material.

5.1 | Analysis for internal stress of work roll

With the aid of previous roll failures experienced in industries,[6–8] the fatigue failure risk will be evaluated at the critical region. The maximum and minimum values of σ_r during a roll rotation can be the driving force causing the internal fatigue. Figure 10 illustrates critical positions denoted by $B^{270}_{09\tilde{0}0}\big|_{\theta=-90^\circ}$, $B^{270}_{09\tilde{0}0}\big|_{\theta=90^\circ}$, $B^{270}_{09\tilde{0}0}\big|_{\theta=0^\circ}$, $C^{0}_{09\tilde{0}0}\big|_{\theta=90^\circ}$, and $C^{0}_{09\tilde{0}0}\big|_{\theta=0^\circ}$, which are based on the previous roll failure experience. Taking $B^{270}_{09\tilde{0}0}\big|_{\theta=-90^\circ}$ as an example, superscript 270 represents the HSS/DCI boundary $r = 270\,mm$, and subscript $09\tilde{0}0$ represents $z = 09\tilde{0}0\,mm$. At those critical positions, consider the effects of the line force p_S^{ave} from the rolled steel $(\theta = -90^\circ)$ and the line force p_B^{ave} from the backup roll $(\theta = 90^\circ)$. The σ_r variation during a roll rotation can be evaluated from the results at $B^{270}_{09\tilde{0}0}\big|_{\theta=-90^\circ}$, $B^{270}_{09\tilde{0}0}\big|_{\theta=90^\circ}$, $B^{270}_{09\tilde{0}0}\big|_{\theta=0^\circ}$, $C^{0}_{09\tilde{0}0}\big|_{\theta=90^\circ}$, and $C^{0}_{09\tilde{0}0}\big|_{\theta=0^\circ}$.

Figure 11 shows the variation of σ_r in the z-direction on the HSS/DCI boundary. Along the line $\theta = 0^\circ$, the stress σ_r is almost constant and close to zero during $z = 0 - 900\,mm$. The maximum stress is $\sigma_{max}^{\theta=0^\circ} = 4\,MPa$ at $z = 0$. In Figure 11, the stress amplitude σ_a controlling the fatigue fracture during a rotation can be discussed by comparing the results at $\theta = -90^\circ$, 0°, and 90°. A larger stress amplitude σ_a can be provided from the rolled steel side line $\theta = -90^\circ$ in the range $0 \le z \le 600\,mm$. Another larger stress amplitude σ_a the backup roll side line $\theta = 90^\circ$ in the range $600\,mm \le z \le 900\,mm$. Here, $z = 600\,mm$ is the intersection of the two stress distributions. The minimum stress from the rolled steel side $(\theta = -90^\circ)$ is $\sigma_{min}^{\theta=-90^\circ} = -602\,MPa$ at $z = 0$; and therefore, the maximum stress amplitude is $\sigma_a^{max} = \sigma_{max}^{\theta=0^\circ} - \sigma_{max}^{\theta=-90^\circ} = 606\,MPa$. This position $(r,z) = (270\,mm, 0)$ is represented by B_0^{270}. Mean stress $\sigma_m = -299\,MPa$ and stress amplitude $\sigma_a = 303\,MPa$ at this point B_0^{270}. On the other hand, the minimum stress from

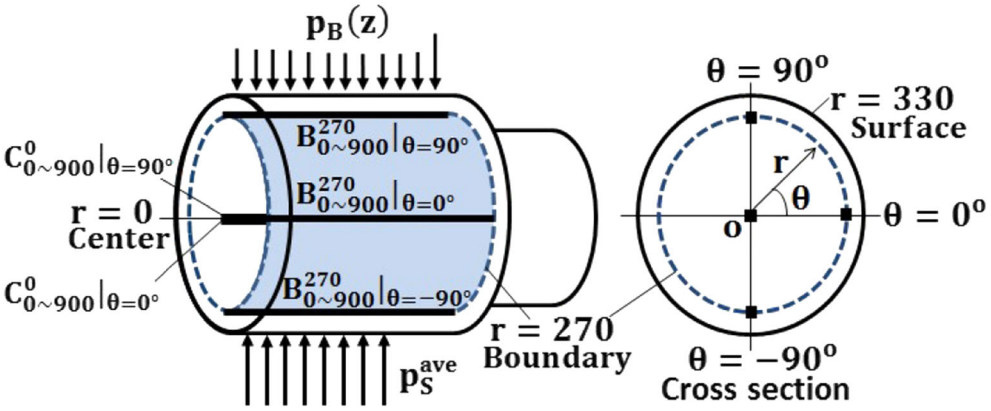

FIGURE 10 Critical position caused by the variation of σ_r in the work roll [Colour figure can be viewed at wileyonlinelibrary.com]

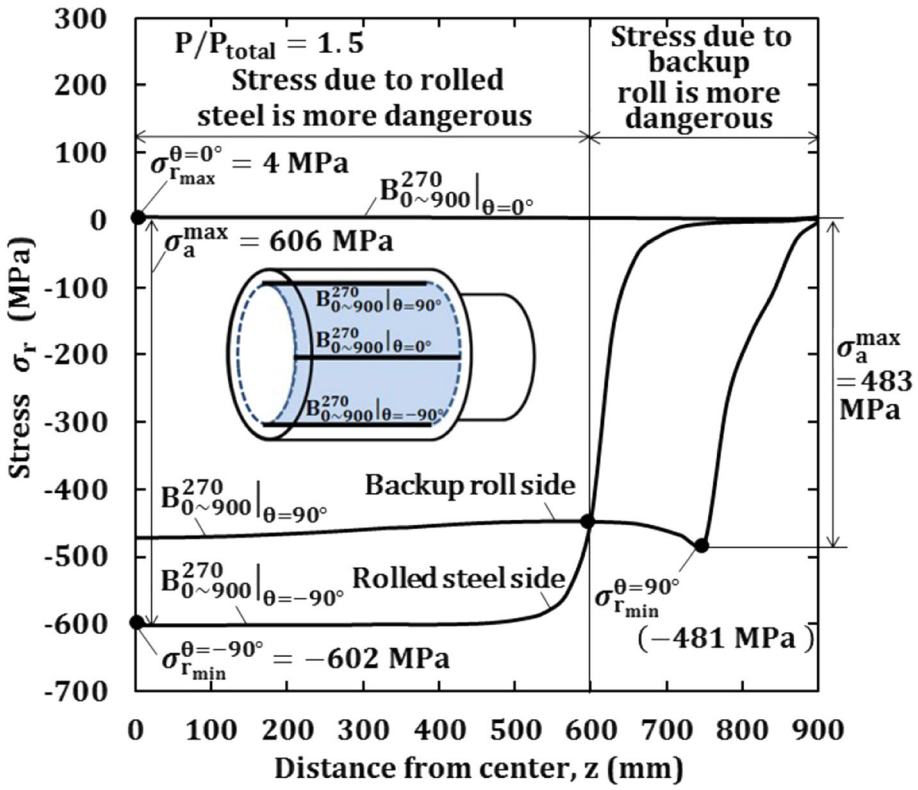

FIGURE 11 Rolling stress σ_r at $\theta = 0^o$, $\theta = 90^o$, and $\theta = -90^o$ along z-direction on the boundary $r = 270$ mm of the work roll when $P/P_{total} = 1.5$ [Colour figure can be viewed at wileyonlinelibrary.com]

the backup roll side $(\theta = 90°)$ is $\sigma_{min}^{\theta=90°} = -481$ MPa at $z = 750$ mm; and therefore, the maximum stress amplitude is $\sigma_a^{max} = \sigma_{max}^{\theta=0°} - \sigma_{min}^{\theta=90°} = 483$ MPa. This position $(r,z) = (270\,\text{mm}, 750\,\text{mm})$ is represented by B_{750}^{270} where the mean stress $\sigma_m = -240$ MPa and stress amplitude $\sigma_a = 242$ MPa.

Figure 12 shows the stress distribution σ_r over the circumference of the work roll on the HSS/DCI boundary $r = 270$ mm. At $z = 0$ denoted by the solid line, the maximum compressive stress σ_r is generated on the rolled steel side, and the second maximum compressive stress σ_r is generated on the backup roll side. When $z = 750$ mm denoted by the dotted line, the maximum compressive stress σ_r is generated only on the backup roll side.

Next, considering failure from the roll central portion experienced previously, the stress amplitude at the work roll center $(r,z) = (0,0)$ is considered in Figure 13. At the center $(r,z) = (0,0)$, maximum tensile stress $\sigma_{max}^{\theta=90°} = 46$ MPa, maximum compressive stress $\sigma_{min}^{\theta=0°} = -85$ MPa$(\theta = 0°)$, and maximum stress amplitude $\sigma_a^{max} = 131$ MPa. The center $(r,z) = (0,0)$ is denoted by C_0^0. Mean stress $\sigma_m = -20$ MPa and stress amplitude $\sigma_a = 67$ MPa at this point C_0^0.

Results from Figure 11 to Figure 13 reveal that the three points inside the roll are under the compressive stress field. Therefore, the fatigue limit lines under compressive stress will be considered in the next section to evaluate the fatigue failure risk.

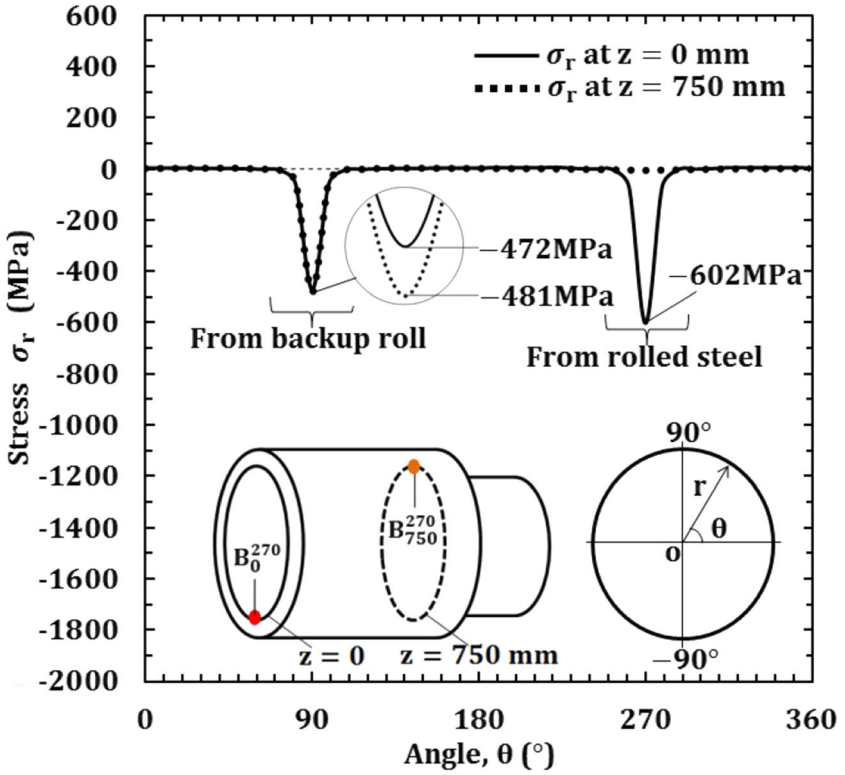

FIGURE 12 Stress distribution σ_r at the boundary along θ-direction at z = 0 and z = 750 mm when $P/P_{total} = 1.5$ [Colour figure can be viewed at wileyonlinelibrary.com]

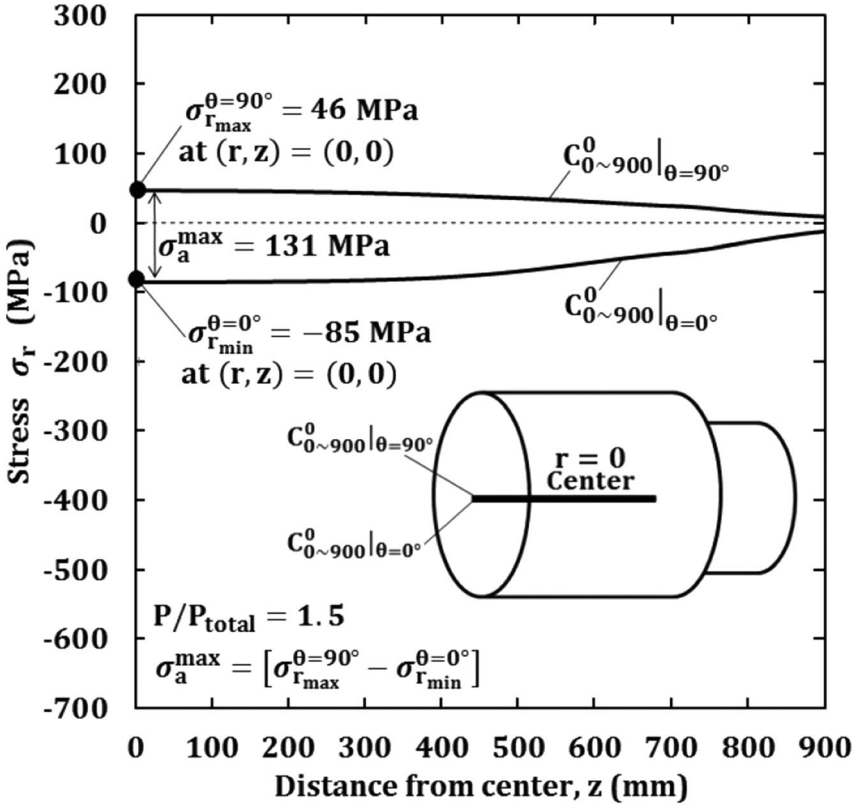

FIGURE 13 Rolling stress σ_r at θ = 0° and θ = 90° along z-direction at the work roll center r = 0 when $P/P_{total} = 1.5$

5.2 | Previous fatigue study under repeated compressive stress

Fatigue failure under large compressive stress was treated by several previous papers, but usually they considered rolling contact fatigue in ball/roller bearings and backup roll surface spalling.[20,21] In other words, few data are available for ordinary fatigue strength under large compressive stress fields.[22] The fatigue life consists of (1) a crack initiation period, (2) crack growth period, and (3) finally ultimate failure. Then, the following information are known regarding such fatigue life under the compressive mean stress.[23–25] Figure 14 illustrates three types of compressive alternative loading under the mean stress $\sigma_m < 0$ when (a) $\sigma_a + \sigma_m = \sigma_{max} > 0$), (b) $\sigma_a + \sigma_m = \sigma_{max} = 0$, and (c) $\sigma_a + \sigma_m = \sigma_{max} < 0$.

1. During the crack initiation stage, the fatigue life is controlled by the stress amplitude irrespective of the mean stress, positive or negative. Under the fixed stress amplitude as shown in Figure 14A–C, the crack initiates at the same time.[23]
2. Instead, during the crack growth stage, with decreasing the mean stress, the crack growth rate decreases

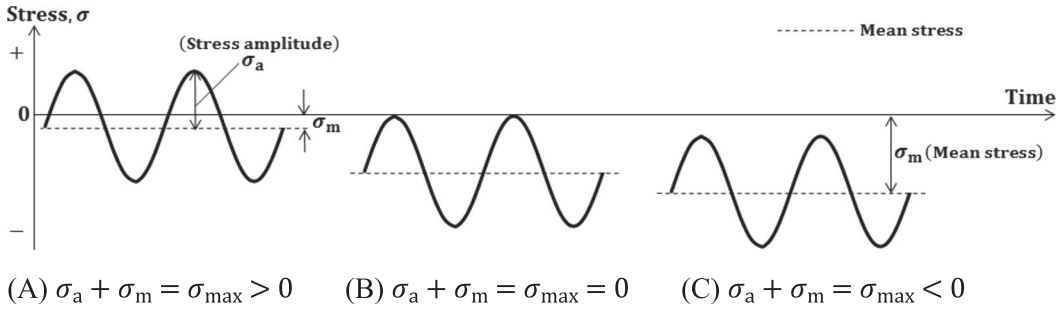

FIGURE 14 Three types of compressive alternative loading where the mean stress $\sigma_m < 0$ when (A) $\sigma_a + \sigma_m = \sigma_{max} > 0$, (B) $\sigma_a + \sigma_m = \sigma_{max} = 0$, and (C) $\sigma_a + \sigma_m = \sigma_{max} < 0$

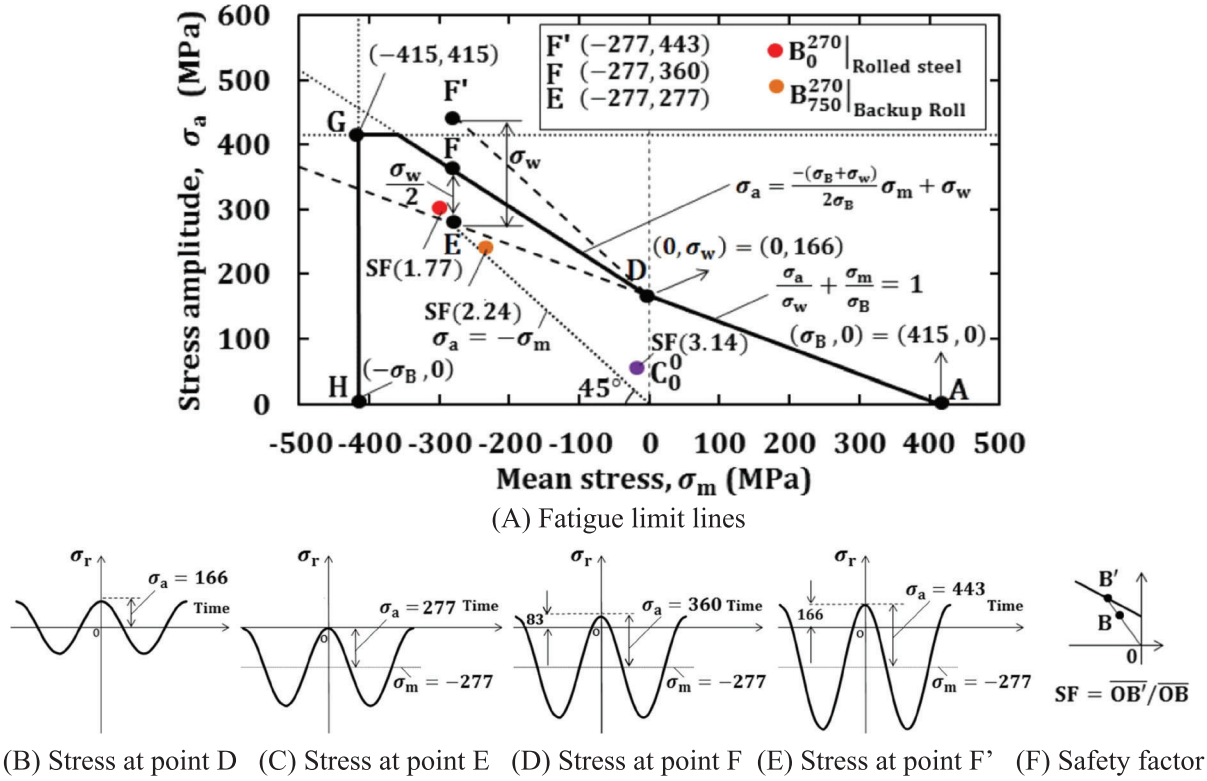

FIGURE 15 (A) Fatigue limit lines to evaluate three critical points B_0^{270}, B_{750}^{270}, and C_0^0 when $P/P_{total} = 1.5$; (B) stress at Point D; (C) stress at Point E; (D) stress at Point F; (E) stress at Point F′; (F) safety factor definition [Colour figure can be viewed at wileyonlinelibrary.com]

sensitively, and the fatigue life increases significantly. It is known that under $\sigma_{max}=0$ in Figure 14B and $\sigma_{max}<0$ in Figure 14C, the crack does not propagate and no final failure.[23,24]

3. However, under $\sigma_{max}>0$ in Figure 14A, the amount of tensile stress $\sigma_{max}=\sigma_a+\sigma_m>0$ necessary for the final failure is not known. It has not been discussed yet until now, and it must vary depending on the magnitude of $\sigma_m<0$.

5.3 | Stress amplitude vs mean stress diagram ($\sigma_a-\sigma_m$ diagram) for compressive mean stress

In this study, the fatigue limit lines are newly prescribed under large compressive stress because no study is available. During the real use of work roll, thermal crack initiations are commonly observed at the roll surface; usually, they do not propagate due to the compressive residual stress introduced at the roll surface. In this way, the previous studies for compressive fatigue described in Section 5.2 can be applied to the real rolls. Figure 15 shows a stress amplitude versus mean stress diagram ($\sigma_a-\sigma_m$ diagram) to discuss the fatigue limit under large compressive alternative loading $\sigma_m\le 0$. First of all, assume the ultimate tensile strength σ_B can be applied to the compressive stress $\sigma_m<0$ and alternative stress $\sigma_a>0$ as express in Equation 8.

$$|\sigma_m|<\sigma_B,\ |\sigma_a|<\sigma_B \tag{8}$$

The so-called modified Goodman law can be expressed in Equation 9 for $\sigma_m\ge 0$.

$$\frac{\sigma_a}{\sigma_w}+\frac{\sigma_m}{\sigma_B}\le 1 \tag{9}$$

Assume this limit line $\sigma_a/\sigma_w+\sigma_m/\sigma_B=1$ can be extended to the negative region $\sigma_m<0$.[26]

Consider pulsating compressive loading $\sigma_a+\sigma_m=\sigma_{max}=0$ as illustrated in Figure 15C. In Figure 15A, the line is indicated as $\sigma_m=-\sigma_a$ denoted by a dotted line with an angle of 45° from the ordinate from the origin. As described in Section 5.2, no final failure happens in the region described by Equation 10.

$$\sigma_a+\sigma_m=\sigma_{max}\le 0 \tag{10}$$

Denote the intersection $\sigma_a/\sigma_w+\sigma_m/\sigma_B=1$ and $\sigma_a+\sigma_m=0$ as Point E as shown in Figure 15A. Because Point E satisfies Equation 10, there is no final failure. Therefore, by adding a certain amount of positive tensile stress, Point F and Point F′ are newly considered.[27] Regarding the fully reversed loading, the fatigue limit is known as Point D as shown in Figure 15B. Point D can be the fatigue limit under the maximum tensile stress $\sigma_{max}=\sigma_m+\sigma_a=166\,\text{MPa}$ and the maximum compressive stress $\sigma_{min}=\sigma_m-\sigma_a=-166\,\text{MPa}$. Instead, at Point E, as shown in Figure 15C, the maximum tensile stress $\sigma_{max}=\sigma_m+\sigma_a=0$ but the maximum compressive stress $\sigma_{min}=\sigma_m-\sigma_a=-554\,\text{MPa}$ is more than three times larger than the compressive stress of point D, $\sigma_{min}=-166\,\text{MPa}$, because $\sigma_{min}=-554\,\text{MPa}=-277\,\text{MPa}\times 2<-166\,\text{MPa}\times 3=-498\,\text{MPa}$. Therefore, at Point E, even with no crack propagation and no final failure, more severe damage is accumulated regarding crack initiation compared with Point D. Because it is known that $\sigma_{max}=0$ at Point E, a certain amount of tensile stress $\sigma_{max}=\sigma_a+\sigma_m>0$ is necessary for the final failure. In other words, Point E cannot be the fatigue limit because $\sigma_{max}=0$ and requires a certain amount of the tensile stress $\sigma_{max}=\sigma_a+\sigma_m>0$ to be the fatigue limit.

Consider F′ whose maximum tensile stress $\sigma_{max}=166\,\text{MPa}$ is the same as Point D as shown in Figure 15E. Due to the larger compressive stress $\sigma_{min}=-554\,\text{MPa}$ at Point E compared with the one $\sigma_{min}=-166\,\text{MPa}$ at Point D, the tensile stress necessary for the fatigue limit can be smaller than $\sigma_{max}=166\,\text{MPa}$. Instead, at Point E, there is no tensile stress; therefore, there is no crack propagation and no final failure as the previous studies indicated.[23–25] In this way, it is found that the fatigue limit at Point F should be between Point D and Point F′. In this study, therefore, half value $\sigma_w/2=83\,\text{MPa}$ is assumed for this tensile stress at Point F as shown in Figure 15D. By drawing the line through Point D and Point F in Figure 15A, the fatigue limit can be estimated. The range can be expressed by the following equation.

$$\sigma_a\le-\frac{\sigma_B+\sigma_w}{2\sigma_B}\sigma_m+\sigma_w \tag{11}$$

For large compressive alternative loading, the fatigue limit is determined by Equations 8–11, which is expressed by the thick solid lines passing through Points A, D, F, G, and H in Figure 15A.

5.4 | Fatigue risk evaluation based on stress amplitude vs mean stress diagram

Based on the fatigue limit lines determined from Equations 8 to 11, the fatigue failure risk can be evaluated. As shown in Figure 15A, three critical points

TABLE 2 Safety factor SF obtained by superposing the residual stress in previous study[28,29] upon the rolling stress in this study when $P/P_{total} = 1.5$

Point	Mean stress σ_m in this study (MPa)	Residual stress σ_{res} in previous study[28,29] (MPa)	$\sigma_m + \sigma_{res}$ (MPa)	Safety factor, SF
$B_0^{270}\big\vert_{\text{Rolled steel}}$	−299	(After quenching) 132	−167	0.89
		(After tempering 1) 126	−173	0.91
		(After tempering 2) 113	−186	0.96
$B_{750}^{270}\big\vert_{\text{Backup roll}}$	−240	(After quenching) 137	−105	0.98
		(After tempering 1) 123	−119	1.04
		(After tempering 2) 85	−157	1.24

described in Section 5.1 are plotted as $B_0^{270}\big\vert_{\text{Rolled steel}}$, $B_{750}^{270}\big\vert_{\text{Backup roll}}$, and C_0^0. The results show that fatigue risk at the point C_0^0 is comparatively smaller although some roll failures were reported at this roll center. This is because some defects tend to appear at the roll center. During casting process, the central portion of the roll is the last portion to solidify. Therefore, impurities and gases are more likely to remain, and defects are more likely to occur at the roll center compared with any other portions. In Appendix C, the risk of fatigue failure at C_0^0 is discussed by considering the residual stress and assuming the defect dimension.

The safety factor is defined as $SF = \overline{OB'}/\overline{OB}$ in Figure 15F. The safety factor evaluation for the critical point B_0^{270} is 1.77, point B_{750}^{270} is 2.24, and point C_0^0 is 3.14. A larger SF value means the point is relatively safer than another point having a smaller SF value. Therefore, the safety factor SF can be used to evaluate the risk of fatigue failure relatively. Although the safety factor $SF \geq 1$, $B_0^{270}\big\vert_{\text{Rolled steel}}$ is relatively more dangerous than $B_{750}^{270}\big\vert_{\text{Backup roll}}$ and C_0^0. The results showed that the fatigue crack initiation around points B_0^{270} on the HSS/DCI boundary may explain several roll failures that previously occurred.

5.5 | Fatigue risk evaluation based on stress amplitude versus mean stress diagram superposing roll residual stress

In Section 5.4, the fatigue risk was evaluated by clarifying the rolling stress appearing inside of the bimetallic work rolls with no residual stress when the work roll is used in a four-high rolling mill. In this section, by superposing the residual stress,[28,29] the final fracture risk is discussed at the same critical points $B_0^{270}\big\vert_{\text{Rolled steel}}$ and $B_{750}^{270}\big\vert_{\text{Backup roll}}$. In Appendix A, the residual stress simulation is briefly introduced because the detail was reported in the previous papers.[5,28–30] Table 2 shows the superposed mean stress $\sigma_m + \sigma_{res}$ from the rolling stress σ_m obtained in this study and the residual stress σ_{res} in Appendix A.[28,29] In Table 2, the residual stresses are considered after quenching, after first tempering, and after second tempering when $P/P_{total} = 1.5$. Table 2 shows that the tensile residual stress can be reduced by 33% from quenching to first tempering and 54% from quenching to second tempering. The small SF values suggest that those critical points on the HSS/DCI boundary may contribute to several previous roll failures.

The method of superposition may have some errors because of the nonlinearity caused by the rolling contact analysis. As shown in Appendix B, therefore, a consecutive FEM analysis for the rolling stress is also performed after the roll residual stress analysis. Figure B1 in Appendix B shows that the SF obtained by the superposition coincides with the SF obtained by the consecutive analysis with less than 13%. It should be noted that the SF values obtained by the consecutive analysis are larger than the superposition SF values. Therefore, the method of superposition can be used conveniently to evaluate the risk a bit more severely.

6 | CONCLUSION

In this study, to clarify the rolling stress, a 3D finite element elastoplastic contact analysis was applied to the work roll in the four-high rolling mill. Then, the risk of internal fatigue failure was newly studied based on the stress during the rolling. To clarify the rolling stress near the HSS/DCI boundary, no residual stress was assumed in this study. Assume the following rolling conditions that can be regarded as the average values in present steelworks[8]: the work roll diameter $D_W = 660$ mm with the length $L = 1800$ mm, the high chrome steel backup

roll diameter of $D_B = 1400\,mm$ with the length $L = 1800\,mm$, the width of the rolled steel $W = 1200\,mm$, and the standard rolling force $P_{total} = 16400\,kN$.[8,9] Then, the conclusions obtained can be summarized in the following way.

1. The fatigue strength under compressive mean stress region was newly considered on the stress amplitude versus mean stress diagram. Then, the fatigue limit lines were proposed based on the fact that the final failure never occurs at the pulsating compressive loading state.
2. With the aid of the previous roll failures experienced in industries, three critical points were chosen on the basis of the analysis and experience over the whole roll geometry. It may be concluded that the most critical point is located at the HSS/DCI boundary point B_0^{270} where $(r,z) = (270\,mm, 0)$ because the largest stress amplitude is caused by the rolling steel. Another critical point is located at B_{750}^{270} where $(r,z) = (270\,mm, 750\,mm)$ due to the contact of the backup roll.
3. The fatigue failure risk was discussed through the relative safety factor SF defined on the stress amplitude versus mean stress diagram. The results showed that the fatigue crack initiation around points B_0^{270} and B_{750}^{270} on the HSS/DCI boundary may cause several roll failures previously occurred in industries.
4. The result showed that fatigue risk at the point C_0^0 was comparatively smaller although some roll failures were reported at this roll center. The result of C_0^0 indicated in this paper can be used conveniently by taking into account the residual stress and the material defect at this point.

ACKNOWLEDGMENT

The authors appreciate Dr. Tetsuro Hidaka for his valuable and useful comments that greatly improved the manuscript. This research did not receive any specific grant from funding agencies in the public, commercial, or not-for-profit sectors.

CONFLICT OF INTEREST

The authors declare that they have no known competing financial interests or personal relationships that could have appeared to influence the work reported in this paper.

AUTHOR CONTRIBUTIONS

M.R.A. wrote the paper; N.A.N. supervised the research; Y.S. proposed and advised the research; K.T., S. Z., and Y.Z. performed the FEM simulation.

DATA AVAILABILITY STATEMENT

The data that support the findings of this study are available on request from the corresponding author. The data are not publicly available due to privacy or ethical restrictions.

NOMENCLATURE

B_0^{270}	critical point on HSS/DCI boundary where $(r,z) = (270\,mm, 0)$
B_{750}^{270}	critical point on HSS/DCI boundary where $(r,z) = (270\,mm, 750\,mm)$
$B_{09\tilde{0}0}^{270}\big\|_{\theta=-90^\circ}$	critical point on HSS/DCI boundary where $(r,z) = (270\,mm, 09\tilde{0}0\,mm)$ from the rolled steel side $(\theta = -90^\circ)$
$B_{09\tilde{0}0}^{270}\big\|_{\theta=90^\circ}$	critical point on HSS/DCI boundary where $(r,z) = (270\,mm, 09\tilde{0}0\,mm)$ from the backup roll side $(\theta = 90^\circ)$
$B_{09\tilde{0}0}^{270}\big\|_{\theta=0^\circ}$	critical point on HSS/DCI boundary where $(r,z) = (270\,mm, 09\tilde{0}0\,mm)$ at $\theta = 0^\circ$
C_0^0	critical point at center point where $(r,z) = (0,0)$
$C_{09\tilde{0}0}^{0}\big\|_{\theta=90^\circ}$	critical point at center point where $(r,z) = (0, 09\tilde{0}0\,mm)$ at $\theta = 90^\circ$
$C_{09\tilde{0}0}^{0}\big\|_{\theta=0^\circ}$	critical point at center point where $(r,z) = (0, 09\tilde{0}0\,mm)$ at $\theta = 0^\circ$
DCI	ductile casting iron
D_W	work roll diameter (mm)
D_B	backup roll diameter (mm)
FEM	finite element method
Grain/FC	grain graphite/flaky graphite cast iron
HSS	high-speed steel
h_c	crown profile height at the backup roll surface (mm)
h_w	wear profile depth at the work roll surface (mm)
L	length of work roll and backup roll (mm)
P	total rolling force defined in Equation (5)
P_{total}	fixed total rolling force (kN)
p_B^{ave}	average line force from backup roll side (kN/mm)
p_S^{ave}	average line force from rolled steel side (kN/mm)
$P_B(z)$	line force from backup roll (kN/mm)
r	radius (mm)
SF	safety factor defined as $SF = \overline{OB'}/\overline{OB}$ in Figure 15F
W	width of the rolled steel (mm)
x,y,z	Cartesian coordinate system
z_1	end point of the contact length in z-direction (mm)
θ	angle (°)
θ_1	contact angle in θ-direction (°)

ℓ_a	length of the curved part of the work roll (mm)
ℓ_b	length of the curved part of the backup roll (mm)
ℓ_c	chamfer length at the backup roll surface (mm)
σ_r	radial stress (MPa)
σ_z	axial stress (MPa)
σ_θ	tangential stress (MPa)
$\sigma_{max}^{\theta=0^\circ}$	maximum stress at $\theta = 0^\circ$ (MPa)
$\sigma_{min}^{\theta=-90^\circ}$	minimum stress at $\theta = -90^\circ$ (MPa)
$\sigma_{min}^{\theta=90^\circ}$	minimum stress at $\theta = 90^\circ$ (MPa)
σ_a	stress amplitude (MPa)
σ_m	mean stress (MPa)
σ_a^{max}	maximum stress amplitude (MPa)
σ_w	fatigue limit stress (MPa)
σ_B	ultimate tensile strength (MPa)
δ	roll deflection (mm)
$\Delta\delta$	backup roll's bending deformation (mm)
τ_{rz}	surface shear stress
R	stress ratio is defined as the ratio of minimum stress to maximum stress
H_V	Vickers hardness
ΔK_{th}	threshold stress intensity factor

ORCID

Mohd Radzi Aridi https://orcid.org/0000-0001-6181-7784

Nao-Aki Noda https://orcid.org/0000-0002-6044-6974

REFERENCES

1. Goto K, Matsuda Y, Sakamoto K, Sugimoto Y. Basic characteristics and microstructure of high-carbon high speed steel rolls for hot rolling mill. *ISIJ Int.* 1992;32(11):1184-1189.
2. Kang YJ, Oh JC, Lee HC, Lee S. Effect of carbon and chromium additions on the wear resistance and surface roughness of cast high-speed steel rolls. *Metall Mater Trans A*. 2001;32(10):2515-2525.
3. Park JW, Lee HC, Lee S. Composition, microstructure, hardness, and wear properties of high-speed steel rolls. *Metall Mater Trans A*. 1999;30(2):399-409.
4. Sano Y, Hattori T, Haga M. Characteristics of high-carbon high speed steel rolls for hot strip mill. *ISIJ Int.* 1992;32(11):1194-1201.
5. Noda NA, Sano Y, Aridi MR, Tsuboi K, Oda N. Residual stress differences between uniform and non-uniform heating treatment of bimetallic roll: effect of creep behavior on residual stress. *Metals*. 2018;8(11):1-10, 952.
6. Sano Y, Kimura K. Statistical analysis about crack and spalling on work roll for hot strip mill finishing rear stands. *Tetsu-to-Hagane*. 1987;73(9):78-85.
7. Sano Y. Fatigue failure problem in the inside of roll body for hot strip rolling-crack initiation problem and its estimation in the actual plant. Paper presented at: The 245th JSMS Committee on Fatigue of Materials and The 36th JSMS Committee on Strength Design · Safety Evaluation, The Society of Materials Science. 1999; Kyoto, Japan.
8. Sano Y. Recent technology for rolling steel and non-ferrous metals. Paper presented at: The 93rd Lecture on Technology of Plasticity, J. Jpn Soc. Technol. Plasticity; 2004; Nagoya, Japan.
9. Sakai H, Noda NA, Sano Y, Zhang G, Takase Y. Numerical solution on interfacial creep generation for shrink-fitted bimetallic roll. *ISIJ Int.* 2019;105(5):889-894.
10. Recent hot strip manufacturing technology in Japan. Tokyo: The Iron and Steel Institute of Japan; 1986.
11. Hamada S, Sakoda Y, Sasaki D, Ueda M, Noguchi H. Evaluation of fatigue limit characteristics of lamellar pearlitic steel in consideration of microstructure. *Soc Mater Sci*. 2011;9(9):790-795.
12. Sekimoto Y, Tanaka K, Nakajima K, Kawanami T. Effects of rolling condition on the surface temperature of work roll in hot strip mill. *Tetsu-to-Hagane*. 1975;61(10):2337-2349.
13. Sekimoto Y. Material and lifespan of hot rolling rolls. *J Jpn Soc Technol Plasticity*. 1982;23:952-957.
14. Li CS, Yu HL, Deng GY, Liu XH, Wang GD. Numerical simulation of temperature field and thermal stress field of work roll during hot strip rolling. *J Iron Steel Res Int*. 2007;14(5):18-21.
15. Schroder KH. Heavy spalls originating in the cores of high chromium rolls. *Metallurgical Plant and Technology*. 1986;2:62-66.
16. Li H, Jiang Z, Tieu KA, Sun W. Analysis of premature failure of work rolls in a cold strip plant. *Wear*. 2007;263(7-12):1442-1446.
17. Pantazopoulos G, Vazdirvanidis A. Fractographic and metallographic study of spalling failure of steel straightener rolls. *J Fail Anal Prev*. 2008;8(6):509-514.
18. Dong Q, Cao JG, Li HB, Zhou YS, Yan TL, Wang WZ. Analysis of spalling in roughing mill backup rolls of wide and thin strip hot rolling process. *Steel Res Int*. 2015;86(2):129-136.
19. Johnson KL. *Contact Mechanics*. Cambridge University Press; 2003.
20. Sakai T, Lian B, Takeda M, et al. Statistical duplex S-N characteristics of high carbon chromium bearing steel in rotating bending in very high cycle regime. *Int J Fatigue*. 2010;32(3):497-504.
21. Zalnezhad E, Sarhan AAD, Jahanshahi P. A new fretting fatigue testing machine design, utilizing rotating-bending principle approach. *Int J Adv Manuf Technol*. 2014;70(9-12):2211-2219.
22. Schroder KH. *A Basic Understanding of the Mechanics of Rolling Mill Rolls*. Austria Eisenwerk Sulzau-Werfen, ESW-Handbook; 2003.
23. Nishitani H, Yamashita N. Effect of mean stress on initiation and growth of fatigue crack in 70/30 brass. *Trans of the JSME*. 1966;32(242):1456-1461.
24. Nisitani H, Goto M. Effect of mean stress on initiation and initial growth of fatigue crack in tension compression fatigue of annealed S45C. *Trans of the JSME*. 1984;50(460):1926-1935.
25. Akiniwa Y, Tanaka K, Taniguchi N. Propagation and non-propagation of short fatigue cracks in notched low-carbon-steel specimen under cyclic compression. *Trans of the JSME*. 1987;53(493):1768-1774.

26. Ince A, Glinka G. A modification of morrow and Smith-Watson-Topper mean stress correction models. *Fatigue Fract Engng Mater Struct*. 2011;34(11):854-867.
27. Kasaba K, Sano T, Kudo S, Shoji T, Katagiri K, Sato T. Fatigue crack growth under compressive loading. *J Nucl Mater*. 1998; 258-263:2059-2063.
28. Noda NA, Hu K, Sano Y, Ono K, Hosokawa Y. Usefulness of non-uniform heating and quenching method for residual stress of bimetallic roll: FEM simulation considering creep behavior. *Steel Res Int*. 2017;88(3):1-11, 1600165.
29. Noda NA, Aridi MR, Torigoe R, Tsuboi K, Sano Y. Reduction of residual stress in bimetallic work roll by tempering. *Journal of the JSTP*. 2020;61(716):183-189.
30. Noda NA, Hu K, Sano Y, Ono K, Hosokawa Y. Residual stress simulation for hot strip bimetallic roll during quenching. *Steel Res Int*. 2016;87(11):1478-1488.
31. Garcia-Granada AA, Smith DJ, Pavier MJ. A new procedure based on Sachs' boring for measuring non-axisymmetric residual stress. *Int J Mech Sci*. 2000;42(6):1027-1047.
32. Kamimiyada K, Konno Y, Yanagitsuru A. Effect of heating conditions before quenching on residual stress in high-speed steel type cast iron rolls by centrifugal cast. *Mater Trans*. 2020; 61(10):1987-1993.
33. Aridi MR, Noda NA, Sano Y, Takata K, Sun Z. Effect of the residual stress to the fatigue failure of the bimetallic work roll in 4-high rolling mill. In: Parinov IA, Chang SH, Kim YH, Noda NA, eds. *Springer Proc. in Materials*. Vol. 10. Springer Nature; 2020:389-393.
34. Hidaka T, Noda NA, Sano Y, Kai N, Fujimoto H. Fatigue strength improvement by replacing welded joints with ductile cast iron joints. *ISIJ Int*. 2019;59(10):1860-1869.
35. Hidaka T, Noda NA, Sano Y, Kai N, Fujimoto H. Lowest fatigue limit estimation of ductile cast iron joints by considering maximum defect size toward replacing welded joints. *ISIJ Int*. 2020;60(5):1006-1015.
36. Murakami Y. *Metal fatigue: Effect of small defects and nonmetallic inclusions*. Elsevier Science; 2002.
37. Yamabe J, Kobayashi M. Effect of hardness and stress ratio on threshold stress intensity factor ranges for small cracks and long cracks in spheroidal cast irons. *J Solid Mech Mater Eng*. 2007;1(5):667-678.
38. Hidaka T. Fatigue strength improvement by replacing welded joints with ductile cast iron joints. Ph.D. Thesis, Kyushu Institute of Technology. 2020.
39. Murakami Y, Matsuda K. Dependence of threshold stress intensity factor range on crack size and geometry, and material properties. *Trans Jpn Soc Mech Eng A*. 1986;52(478):1492-1499.
40. Murakami Y, Endo M. Evaluation method of the effect of micro defects on fatigue strength. *Trans Jpn Soc Mech Eng A*. 1983;49(438):127-136.
41. Murakami Y, Endo M. Effect of hardness and crack geometry on ΔK_{th} of small cracks. *J Soc Mater Sci Jpn*. 1986;35:911-917.
42. Sugiyama Y, Asami K, Matsuoka S. Quantitative evaluation method of fatigue limit of materials with defects and its investigation using ductile cast iron. *Trans Jpn Soc Mech Eng A*. 1992; 58(556):2287-2292.
43. Tamura H, Sugiyama Y, Shiraki N, Matsuzaka K, Umehara T, Usami H. Effect of matrix structure and defect size on fatigue limit of heat-treated spheroidal graphite cast iron. *J JFS*. 2001; 73:605-610.

How to cite this article: Aridi MR, Noda N-A, Sano Y, Takata K, Sun Z, Takase Y. Fatigue failure risk evaluation of bimetallic rolls in four-high hot rolling mills. *Fatigue Fract Eng Mater Struct*. 2022; 1-23. doi:10.1111/ffe.13651

APPENDIX A: RESIDUAL STRESS ANALYSIS OF THE BIMETALLIC WORK ROLL

This study focuses on clarifying the rolling stress assuming the zero residual stress. As the final risk evaluation, however, the residual stress of the work roll should be considered. In this appendix, the outline of residual stress simulation is briefly introduced because the detail was reported in the previous papers.[5,28–30] The internal stress cannot be obtained by the nondestructive methods such as the x-ray diffraction method and ultrasonic method. Therefore, destructive inspections such as Sachs boring method and disk cut method are sometimes applied spending high-cost and time-consuming effort.[31,32] In this sense, the residual stress simulation has been requested to obtain the residual stress distribution from the surface to the inside of the roll under various different heat treatments.

Figure A1 illustrates the surface temperature history of the bimetallic work roll during heat treatment consisting of the preheating, quenching, and tempering. In the preheating process, the whole roll is heated up to the uniform temperature of $T_{Start} = 1050°C$ and kept for several hours. Then, the roll temperature drops rapidly through air cooling. After that, the roll is put into the furnace again and maintained at $T_{Q,Keep}$ to prevent excessive thermal stresses caused by rapid cooling. After this temperature keeping period, the roll is cooled down slowly until to the temperature of $T_{T,Finish}$ where the quenching is finished. After the quenching process, the tempering process is performed two times to release the residual stress and obtained the stable microstructure. After this process, the generated residual stress is used as an initial condition for the consecutive FEM analysis of the rolling analysis.

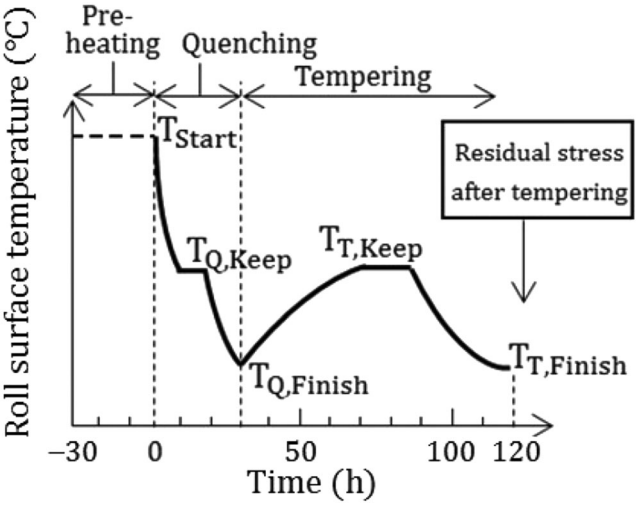

FIGURE A1 Heating, quenching, and tempering treatment of the bimetallic work roll

Predicting the residual stress of the bimetallic roll during preheating, quenching, and tempering can be realized by FEM simulation efficiently with lower cost and higher accuracy compared with experimental measurement. In the previous studies,[5,28–30] axisymmetric FEM model of a half-length of the roll was considered as shown in Figure A2. Figure A3 shows Young's modulus, thermal expansion coefficient, Poisson's ratio, stress–strain characteristic for both DCI and HSS, thermal conductivity, and specific heat during the quenching process. In Figure A4, the stress distributions are shown after quenching, after first tempering, and after second tempering based on the material data in Figure A3. After the first tempering, the maximum tensile stress decreased by 35%, and after the second tempering, the maximum tensile stress decreased by 54%.

APPENDIX B: CONSECUTIVE ROLLING STRESS ANALYSIS OF THE BIMETALLIC WORK ROLL AFTER ANALYZING RESIDUAL STRESS

This study focuses on clarifying the rolling stress assuming the zero residual stress. In Section 5.5, the final fatigue

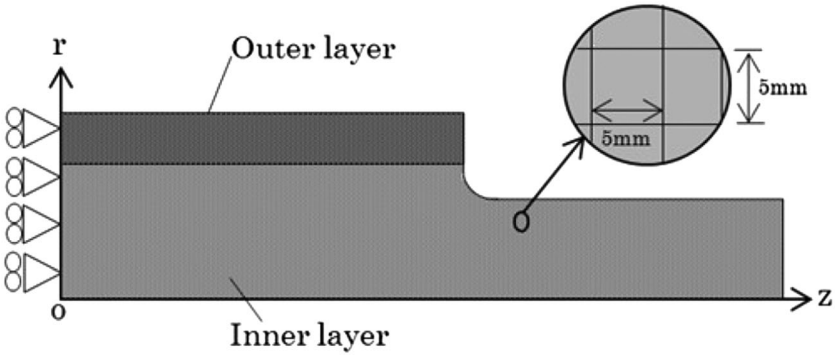

FIGURE A2 Axisymmetric FEM model of the bimetallic work roll to simulate the heating treatment

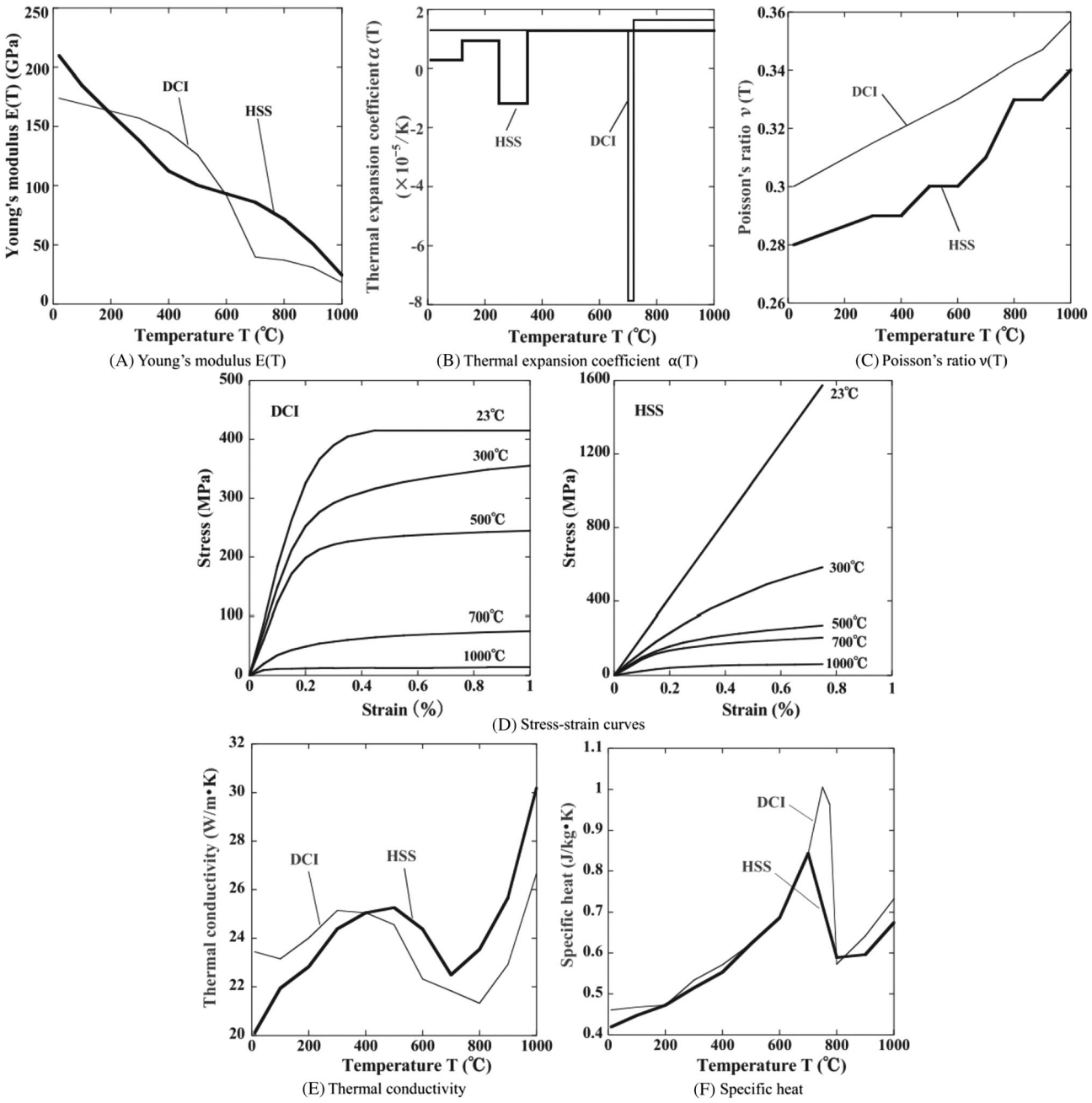

FIGURE A3 (A) Young's modulus; (B) thermal expansion coefficient; (C) Poisson's ratio; (D) stress–strain for DCI and HSS; (E) thermal conductivity; (F) specific heat

risk is evaluated by superposing the residual stress in Appendix A upon the rolling stress in Section 5.4. The method of superposition in Section 5.5 may have some errors because of the nonlinearity caused by the rolling contact analysis. In this appendix, therefore, other analysis results are indicated by performing the consecutive rolling stress analysis after the residual stress simulation. They can be obtained in the following way.[33] First, the residual simulation is performed by using 3D modeling instead of the axisymmetric FEM modeling. Then, after the residual stress is obtained, the consecutive rolling stress starts by using the residual stress as an initial condition. The obtained results are reflecting both residual stress and rolling stress. Figure B1 shows the three critical points' results $B_0^{270}|_{\text{Rolled steel}}$, $B_{750}^{270}|_{\text{Backup roll}}$, and C_0^0 after considering the consecutive FEM rolling analysis. In Figure B1, the safety factor SF for each critical point is also indicated. The SF values obtained by the consecutive analysis are larger than the superposition SF values. Therefore, the method of superposition can be used conveniently to evaluate the risk a bit more severely.

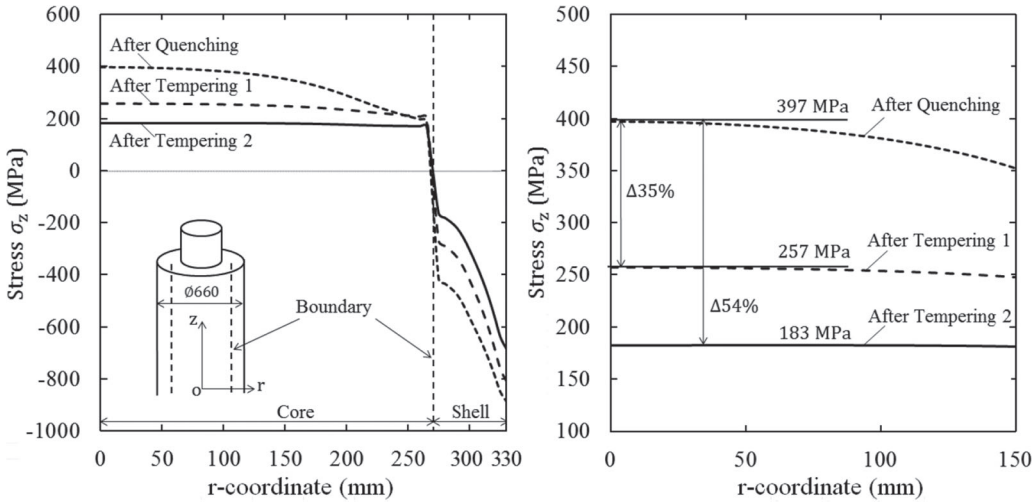

(A) Stress distribution σ_r (B) Details of maximum stress range

FIGURE A4 (A) Stress distributions after quenching, after first tempering, and after second tempering. (B) Details of the maximum stress range

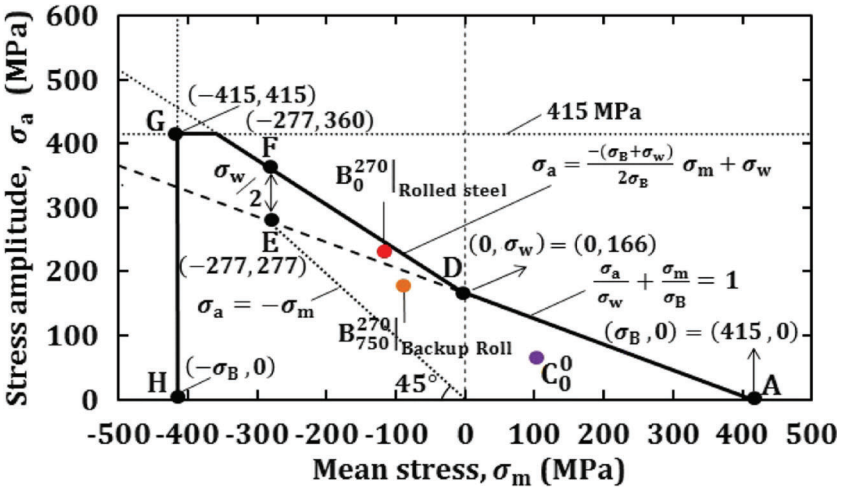

(A) Fatigue limit diagram

Point	Safety factor, SF
$B_0^{270}\|_{\text{Rolled steel}}$	1.09
$B_{750}^{270}\|_{\text{Backup roll}}$	1.43
C_0^0	1.55

(B) Safety factor, SF

FIGURE B1 (A) Fatigue limit diagram of the critical points by considering consecutive FEM rolling analysis. (B) Safety factor SF for the critical points when $P/P_{total} = 1.5$ [Colour figure can be viewed at wileyonlinelibrary.com]

As shown in Figures 15A and B1, although the roll center C_0^0 is relatively safer, several previous roll failures were reported at the roll center. This is because some defects tend to appear often at the roll center. Therefore, the fatigue risk is discussed by considering the defect appearing at the roll center in Appendix C.

APPENDIX C: FATIGUE RISK EVALUATION AT THE ROLL CENTER OF THE BIMETALLIC WORK ROLL ASSUMING DEFECT DIMENSION

As shown in Figure 15 in Section 5.3 and Figure B1 in Appendix B, the point C_0^0 is comparatively safer than the

points B_0^{270} and B_{750}^{270}. During the casting process, however, the central portion of the roll is the last portion to solidify. Therefore, impurities and gases are more likely to remain, and defects are more likely to occur at the roll center compared with any other portions. In this appendix, the fatigue risk at the roll center is discussed by considering such defects. Recently, Hidaka et al estimated the lowest fatigue limit of DCI joint structures toward replacing welded joints.[34,35] In their studies, the effect of the defect on the fatigue limit was considered on three different regions for the pulsating loading with the stress ratio $R = 0$. In a similar way, for cycling loading $R = -1$, Equations C1–C3 can be obtained. Here, in Region I, the fatigue limit is determined from the tensile strength σ_B. In Region II, the fatigue limit is controlled by Vickers hardness H_V. In Region III, because the defect size is larger, the fatigue limit is proportional to the threshold stress intensity factor ΔK_{th}.[36–38]

$$\text{Region I}: \ \sigma_w = 0.4\sigma_B \tag{C1}$$

$$\text{Region II}: \ \sigma_w = \frac{1.56(H_V + 120)}{(\sqrt{area})^{1/6}}, H_V = 106\,\text{kgf/mm}^2 \tag{C2}$$

$$\text{Region III}: \ \sigma_w = \frac{\Delta K_{th}}{1.3\left(\sqrt{\pi\sqrt{area}10^{-6}}\right)}, \Delta K_{th} = 19\,\text{MPa}\sqrt{\text{m}} \tag{C3}$$

In Equations C1–C3, σ_w is in MPa and is the fatigue limit under cycling loading $R = -1$ of a material containing a defect; HV is in kgf/mm^2 and is the Vickers hardness number; $\sqrt{area}$ is in μm and is the square root of defect/crack area projected normal to the maximum principal stress. Figure C1 illustrates the fatigue limit lines expressed by those equations. As shown in Figure C1, the boundary of Regions II and III is $\sqrt{area} \fallingdotseq 12800\,\mu\text{m}$.

Figure C2 illustrates the fatigue limit σ_w when the spheroidal defect diameter $2a = 0, 5000, 10000\,\mu\text{m}$ is assumed.[39–43] The defect size 5 mm (= 5000 μm) is empirically known as a typical defect size for roll maker companies, and for the safety reason, 10 mm (= 10000 μm) defect size is also considered. Because the considered $\sqrt{area}$ is $\sqrt{area} = \sqrt{\pi a^2} = 0, 4431\,\mu\text{m}, 8862\,\mu\text{m} < 12800\,\mu\text{m}$ in Figure C1,

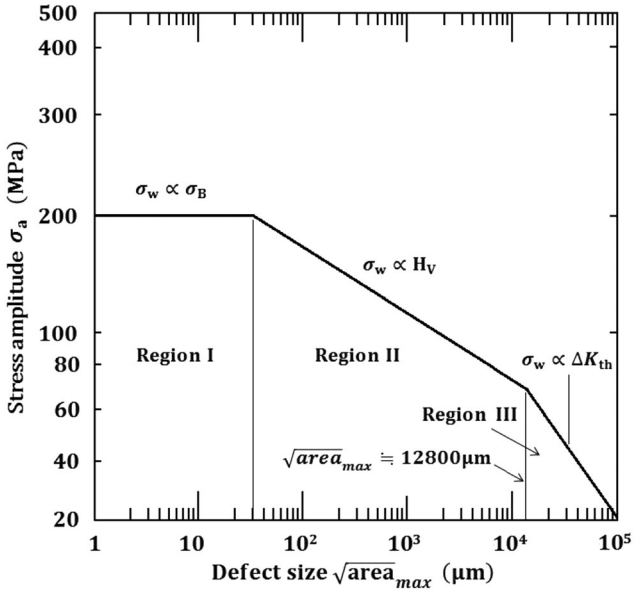

FIGURE C1 The fatigue limit σ_w at point C_0^0 when consider defect size $\sqrt{area}$

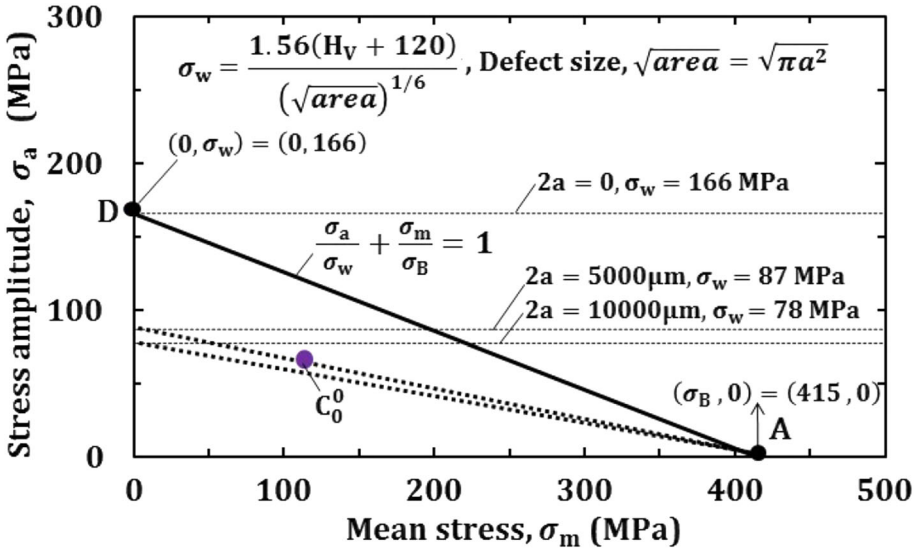

FIGURE C2 Stress amplitude versus mean stress diagram to evaluate the fatigue failure at point C_0^0 when the spheroidal defect diameter $2a = 0, 5000, 10000\,\mu\text{m}$ is assumed through $\sqrt{area} = \sqrt{\pi a^2}$ when $P/P_{total} = 1.5$ [Colour figure can be viewed at wileyonlinelibrary.com]

Equation C2 in Region II can be applied to evaluate σ_w. Figure C2 shows that the fatigue limit σ_w decreases from $\sigma_w = 166\,\text{MPa}$ to $\sigma_w = 87\,\text{MPa}$ by considering Equation C2 when the defect diameter is changed from $2a = 0$ to $2a = 5000\,\mu\text{m}$. When $2a = 10000\,\mu\text{m}$, the fatigue limit σ_w decreases to $\sigma_w = 78\,\text{MPa}$. Table C1 shows that the safety factor SF decreases with increasing the defect size. Figure C2 shows that the point C_0^0 becomes dangerous depending on the defect dimensions. If the defect with 5 mm size exists, the risk of fatigue failure at the point C_0^0 becomes larger than other dangerous points $B_0^{270}|_{\text{Rolled steel}}$ and $B_{750}^{270}|_{\text{Backup roll}}$ from Figure C2 and Table C1.

TABLE C1 Safety factor SF for the critical point C_0^0 when the spheroidal defect diameter $2a = 0, 5000, 10000\,\mu\text{m}$ is assumed through $\sqrt{area} = \sqrt{\pi a^2}$ when $P/P_{\text{total}} = 1.5$

Diameter change (μm)	**Safety factor, SF**
$2a = 0$	1.55
$2a = 5000$	0.98
$2a = 10000$	0.91